Journal of Low Temperature Physics, Vol. 106, Nos. 5/6, 1997

Intrinsic and Extrinsic Mechanisms of Vortex Formation in Superfluid ^{3}He-B

V. M. H. Ruutu, Ü. Parts, J. H. Koivuniemi, N. B. Kopnin,* and M. Krusius

Low Temperature Laboratory, Helsinki University of Technology, 02150 Espoo, Finland

We report on the first comprehensive measurements of critical superflow velocities in ^{3}He-B which allow different mechanisms of vortex formation to be identified. As a function of temperature T *and pressure* P, *we measure the critical angular velocity* $\Omega_c(T, P)$ *at which vortices start to form in slowly accelerating rotation in a cylindrical container filled with ^{3}He-B. Owing to the long coherence length* $\xi(T, P) \sim 10$–100 *nm, either trapped remanent vorticity or intrinsic nucleation may dominate vortex formation, depending on the roughness of the container wall and the presence of loaded traps.*

NMR measurement with a resolution of one single vortex line allows us to distinguish between different processes: (1) Three extrinsic mechanisms of vortex formation have been observed. One of them is the vortex mill, a continuous periodic source which is activated in a rough-walled container well below the limit for intrinsic nucleation. (2) In a closed smooth-walled container intrinsic nucleation is the only mechanism available, with a critical velocity $v_c(T, P) = \Omega_c(T, P)\,R$, *where* R *is the radius of the container. We find* $v_c(T, P)$ *to be related to the calculated intrinsic stability limit* $v_{cb}(T, P)$ *of homogeneous superflow. The existence of this connection in the form of a scaling law implies that nucleation takes place at an instability, rather than by thermal activation or quantum tunneling which become impossible because of an inaccessibly high energy barrier.*

I. INTRODUCTION

A. Intrinsic and Extrinsic Vortex Formation

The concept of a quantized vortex line was introduced in the early fifties by Lars Onsager, Richard Feynman, and others to explain the remarkable properties of flowing superfluid ^{4}He-II.[1–3] Ever since, the puzzle of how

*Permanent address: Landau Institute for Theoretical Physics, 117334 Moscow, Russia.

0022-2291/97/0400-0093$12.50/0

quantized vortices are formed has remained, experimentally at least, a disturbing jungle of contradictions. It is only in the last 5–10 years that new experiments have come to agree with theoretical expectation.

Both intrinsic nucleation and extrinsic processes, which all involve the walls of the container, contribute to vortex formation. In the bulk liquid vortex creation is rare and has only been observed in the presence of ions accelerated through the liquid or under energetic radiation. Comparison of the experimental features controlling vortex creation in the A and B phases of superfluid ^{3}He, in ^{4}He-II, and in superconductors[4] shows many common properties but also emphasises important differences. In ^{3}He superfluids intrinsic nucleation tends to dominate, in ^{4}He-II it is generally bypassed by extrinsic processes with lower energy barriers, and finally in superconductors, which in practice always have a nonideal crystalline lattice, flux line formation is governed by heterogeneous processes. The He superfluids are inherently more ideal systems and traditionally vortex nucleation is preferably studied in a superfluid rather than in a superconductor.

A *singular vortex line*, the conventional type of quantized vorticity, consists of a singular core and the trapped supercurrent, which flows around the core with one quantum of circulation. In the singular core the amplitude of the order parameter deviates from its value in the bulk superfluid; the core has a radius comparable to the superfluid coherence length. The vortex line is a stable topological object of the superfluid order parameter field. This means that it can only be nucleated or annihilated at the boundary of the system and that its two end points remain anchored to the boundary, unless it forms a closed loop.

In the undisturbed superfluid, with no trapped remanent vortices, the creation of a vortex line is inhibited by a nucleation barrier. It is the energy needed for forming a vortex half-ring with the critical radius, *i.e.* a half-ring which is of self-sustained size at the ambient value of the superflow velocity v_s. Therefore the height of the nucleation barrier depends on the externally applied superflow velocity v_s. A number of mechanisms[3,5] have been proposed how the nucleation barrier is overcome and what determines the critical velocity of the superflow. The creation of a vortex line is a process reminiscent of a first order phase transition, in which a bubble of the new phase has to be nucleated with a radius which exceeds a critical value: A bubble beyond the critical radius is over the nucleation barrier and expands spontaneously, driven by the free energy difference between the two phases, while a smaller bubble contracts under the influence of the surface tension from the strongly curved interface. Similarly, a segment of a vortex ring, which is nucleated at the wall of the container, expands only if the force from the superflow threading the loop exceeds the tension in the vortex line (Fig. 1). The energy, which is released when the vortex ring

moves across the stream lines in the flow, is dissipated in the liquid by the interaction of the moving vortex with the normal component, known as mutual friction (Sec. II F). In this process dissipation remains finite and the system stays in thermal equilibrium.

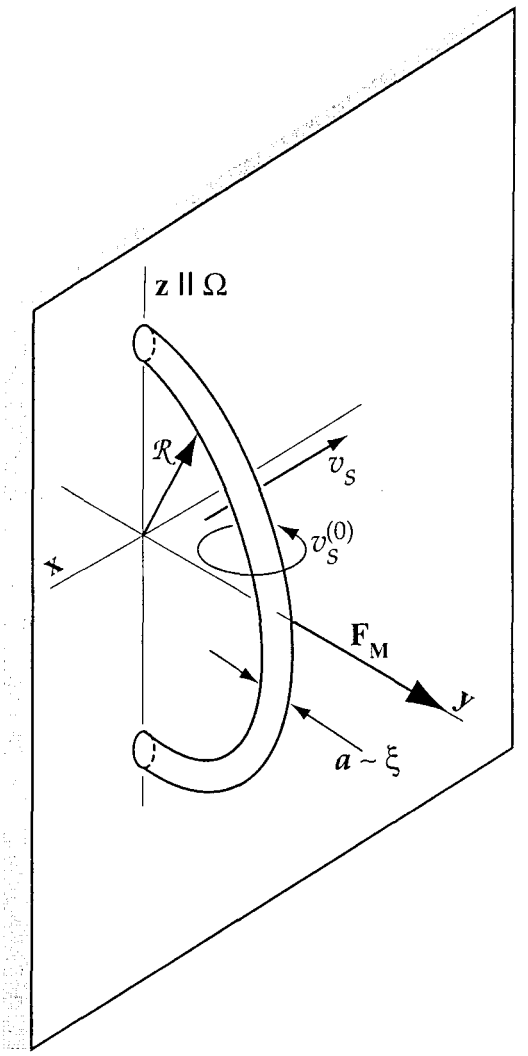

Fig. 1. Nucleating vortex half-ring in uniform superflow at a flat wall. In the equilibrium state, the Magnus force from the superflow is normal to the wall and is opposed by the linear tension (or self-induced flow field).

The bulk superfluid can be arranged to be free of impurities. This is rigorously true for the ^{3}He superfluids while in ^{4}He-II a controlled number of ^{3}He impurity atoms can be dissolved which gives rise to interesting effects in the nucleation properties at the lowest temperatures. Thus we may say that the only deviation from ideal behavior in the superfluids is introduced by the container walls with surface roughness on varying, and generally uncontrolled, length scales.

The walls influence vortex formation in different ways. Rough walls provide sites for the pinning and trapping of remanent vortices. Also at a surface asperity the local superflow velocity is increased from its average value further away in the bulk fluid. Therefore a sharp wedge-shaped asperity may become singled out as the nucleation center where vortex formation starts. In the case of the ^{3}He superfluids a controlled amount of ^{4}He can be administered into the container which phase separates on the walls as a superfluid film or a solid, depending on the pressure, and can be used to influence the superflow properties at the surface.

It has been established in numerous experiments that, in ^{4}He-II, vortex lines are generally created from pre-existing remanent vortex filaments. The trapped vortices start moving at low superflow velocities. They then proliferate by various *extrinsic* processes of vortex formation and thus bypass the *intrinsic* nucleation mechanisms, which would become effective at higher velocities. One has been able to block the extrinsic mechanisms only in measurements with characteristic dimensions of submicron size. In contrast, in superfluid ^{3}He, intrinsic nucleation is observable even in a large container if the walls are sufficiently smooth and remanent vorticity is absent.

In this report we shall discuss measurements on the critical properties of superflow in ^{3}He-B.[6,7] To acquire an understanding of the differences, first between extrinsic and intrinsic processes, and secondly between ^{4}He-II and ^{3}He-B, the next section provides an introduction on critical effects in these two superfluids.

B. Critical Velocities of Superflow

Unattenuated frictionless flow is the most striking manifestation of superfluidity.[3,4] Dissipationless flow is demonstrated by the existence of a persistent supercurrent which, once started, circulates indefinitely in a narrow ring-shaped tube. Dissipation sets in only if the flow velocity exceeds a critical value. There are several mechanisms, associated with the creation of different excitations, which can push superflow to a dissipative state. As suggested by Landau, at zero temperature the spontaneous

emission of excitations becomes energetically favorable at velocities which exceed

$$v_{cL} = \min\{\varepsilon(p)/p\} \tag{1}$$

where $\varepsilon(p)$ is the energy of the elementary excitation with a linear momentum p.

The instability with respect to the production of elementary excitations defines the *Landau critical velocity*. For example, in ^{4}He-II the minimum in Eq. (1) is reached for rotons with $\varepsilon(p_0) \approx 10$ K and $p_0/h \approx 20$ nm^{-1}, which gives $v_{cL} = \varepsilon(p_0)/p_0 \approx 60$ m/s.[3,4] In superfluid ^{3}He-B, the Landau limit is associated with the creation of quasiparticle excitations across the energy gap: $v_{cL} = \Delta/p_F \sim 10$ cm/s, where Δ is the superfluid energy gap and p_F the Fermi momentum.

Quasiparticle excitations, which appear at the Landau limit, do not necessarily lead to continuous dissipation. For example, in Fermi superfluids, such as ^{3}He, the single-particle excitations obey Fermi statistics and fill all energy levels in the region $\varepsilon(p) - \mathbf{p}\mathbf{v}_s < 0$. In stationary flow, an equilibrium state can be established when all levels are filled and no new excitations are created. These excitations now constitute the normal component of the fluid which is in equilibrium and does not give rise to further dissipation.[8] The best illustration is persistent superflow in ^{3}He-A: Here the energy gap Δ vanishes for quasiparticles with their momentum directed along the anisotropy axis of the order parameter, and thus v_{cL} is zero. Nevertheless, dissipation can be absent since, for steady flow in a channel, the equilibrium state is established rather quickly after the emission of the initial excitations. For the same reason, the Landau limit does not necessarily imply that superfluidity is destroyed at higher velocities.

However, when the emission of excitations does not lead to an equilibrium state, supercritical motion is accompanied by dissipation. Nonequilibrium excitations can be produced by moving ions or other small objects, such as a vibrating wire. Experimentally, the Landau velocity has been directly determined from the limiting velocity for the propagation of negative ions in ^{4}He-II[9,10] and in ^{3}He.[11] It has also been determined from the saturation velocity of a vibrating wire in ^{3}He.[12]

In addition to elementary excitations, there may exist excitations specific to the superfluid state. Vortices are the most important example. Ideally superflow is potential, since its velocity

$$\mathbf{v}_s = \frac{\hbar}{m^*} \nabla\phi(\mathbf{r}) \tag{2}$$

is proportional to the gradient of the phase $\phi(\mathbf{r})$ of the superfluid order parameter. Therefore, one expects curl $\mathbf{v}_s = 0$ everywhere in the fluid. However, excitations can appear in the form of a vortex line with a singular core such that the phase ϕ changes by 2π in the bulk fluid on circling once around the core. The elementary excitation corresponds to a vortex ring with radius $\mathscr{R}$. Energy arguments (Sec. IIA) show that the minimum in Eq. (1) is achieved with a ring radius which depends on the external superflow velocity as[3]

$$v_{cF} \approx \frac{\kappa}{4\pi\mathscr{R}} \ln\left(\frac{\mathscr{R}}{a}\right) \tag{3}$$

Here a is the core radius and κ the velocity circulation around the vortex line. We shall consider only vortices with one circulation quantum, when $\kappa = h/m^*$. The mass m^* of the "superfluid particles" is m_4 for ^{4}He-II and $2m_3$ for superfluid ^{3}He, m_3 being the mass of a ^{3}He atom. The velocity v_{cF}, which via its dependence on the ring size $\mathscr{R}$ in practice is determined by the flow geometry, is now commonly called the *Feynman critical velocity*, although Feynman himself originally had a somewhat different process in mind.[2]

At v_{cF} a vortex ring with the radius $\mathscr{R}$ is energetically stable in the flow. At other velocities an existing ring expands or contracts and crosses streamlines if the motion is dissipative at finite temperature. The dissipation is caused by mutual friction, the motion of the vortex through the viscously flowing sea of normal excitations, which couples the superfluid and normal components. In forced superflow with increasing velocity the expansion and reconnection of vortex rings eventually leads to a self-proliferating vortex tangle, to superfluid turbulence.

The container geometry and the different length scales of heterogeneity of its walls determine which size of remanent vortex filament may remain trapped in the container. The largest possible loop has a radius comparable to that of the entire container (or flow tube) with radius R. The critical velocity v_{cF} with the largest possible ring size $\mathscr{R} = R$ in Eq. (3) defines the minimum flow velocity at which the first vortex becomes stable in the superflow. A vortex of shorter length may also exist in the container if it is, say, stretched between two asperities separated by a distance d. When the flow velocity increases, this loop starts to bend until its radius of curvature has decreased to $d/2$. If the flow velocity continues to increase further, next the end points of the semi-circular loop start to move along the surface, while its radius $\mathscr{R} \geq d/2$ increases, and the loop becomes mobile. The critical velocity determined by Eq. (3) with $\mathscr{R} = d/2$ is the *depinning critical velocity* (Sec. IIE): the threshold velocity beyond which a trapped

vortex becomes mobile. Because of the macroscopic quantity $\mathscr{R}$ in the denominator of Eq. (3), the Feynman critical velocity v_{cF} is much lower than the Landau instability limit v_{cL}: the minimum v_{cF} is on the order of 0.01 cm/s for a tube of 1 mm in diameter.

The Feynman velocity, defined in the manner of above, sets the division line when the flow with a vortex ring has smaller energy than the flow without it. It does not imply that vortices are actually created above this limit. In ^{4}He-II the experimentally determined critical velocity v_c is generally on the order of some Feynman velocity v_{cF}, which is characteristic of the measuring set-up. Typically it decreases when the diameter of the flow channel is increased, in qualitative accordance with Eq. (3). A quantitative fit to experimental data is often provided by the empirical relation $v_c \propto 1/R^{1/4}$, if R is taken to be the smallest dimension of the flow channel in the direction perpendicular to the superflow.[5] In channel flow experiments this velocity can be confused with that at which self-sustained dissipation starts. Typically this onset of turbulent superflow is an order of magnitude larger than v_{cF}.

Remanent vortices are believed to be the main source for *extrinsic* vortex formation and the low v_c values which are measured for ^{4}He-II in flow experiments with macroscopic dimensions. The pre-existing trapped vortices may have been formed previously in the presence of supercritical velocities or they may even originate from primordial vortices which are created in a rapid phase transition to the superfluid state.[13-15] Vortices may also be supplied from an external source to the measuring volume or a trapped vortex filament may act as a "vortex mill" in a nonuniform superfluid velocity field, by shedding off vortex loops in an endless succession at some characteristic velocity threshold, i.e. it generates repeatedly a new vortex whenever the flow reaches a critical value.[16,17] In practice, a small size flow channel is helpful in blocking the influence of the viscous normal component and in clamping the motion of any existing vortices because v_{cF} in Eq. (3) increases with decreasing characteristic channel size $R \approx \mathscr{R}$. This is often achieved by packing the flow tube with μm size powder to produce a "superleak" through which only the superfluid component is able to flow.

Extrinsic processes should be distinguished from *intrinsic nucleation* of new vortices which is characterized by orders of magnitude higher critical velocities. Here the nucleation energy barrier has to be overcome in order to form a new vortex ring (Sec. II A). The theory of vortex nucleation was originally formulated by Iordanski,[18] and by Langer and Fisher[19] in terms of thermal activation over the nucleation barrier. The connection with phase slip and dissipation was explained by Anderson.[20] These ideas were worked out in the sixties but it has taken two or three decades to provide convincing experimental proof.

If all extrinsic sources of vorticity are blocked, as seems to be the case for superflow through a submicron-size orifice,[21,22] then at some point in increasing superflow the intrinsic critical velocity will eventually be reached. In the case of ^{4}He-II, this is the velocity at which the nucleation barrier can be surmounted by thermal or quantum fluctuations. For ^{3}He-B the situation is different: the nucleation barrier is so high that it cannot be overcome thermally or quantum-mechanically, and the critical velocity becomes approximately equal to the intrinsic instability limit of bulk superflow.[23] This difference in intrinsic nucleation in the two superfluids is a consequence of the large disparity in their vortex core sizes. The barrier height corresponds approximately to the energy of the smallest possible vortex loop which, in turn, has a length that approaches the core size a.

The following order-of-magnitude argument illustrates the situation in the two superfluids. In ^{4}He-II, the coherence length and the core diameter are of atomic scale. Thus the energy of the shortest initial vortex loop with a size of the order of the core radius is $\mathscr{E}_0 \sim \rho_s \kappa^2 a \sim 10$ K, where ρ_s is the density of the superfluid component. This energy is the barrier height, therefore the probability of thermal and even quantum fluctuations can be quite substantial in ^{4}He-II. In contrast, ^{3}He-B vortices have singular cores with $a \sim \xi$, where the superfluid coherence length ξ is 10^2 to 10^3 times larger and thus $\mathscr{E}_0$ is on the order of 10^3 K. This makes the nucleation barrier extremely high in comparison to the characteristic temperature of the system which, in turn, is 10^3 times lower than in ^{4}He-II. Thus the probability of thermally activated nucleation is vanishingly small in ^{3}He-B: $\mathscr{E}_0/k_B T \gtrsim 10^6$. The barrier height depends on the superflow velocity v_s, but in practice thermally activated nucleation can be neglected up to the intrinsic superflow instability, the threshold at which the barrier vanishes as a function of v_s.

At the superflow instability the energy $\rho_s \kappa^2 a$ of the initial vortex loop becomes equal to the kinetic energy of superflow $\rho_s v_s^2 a^3$ contained within the volume of the loop being formed. Equating these two energies, one obtains the critical velocity at which bulk superflow becomes unstable,

$$v_{cb} \sim \kappa/2\pi a \tag{4}$$

This bulk critical velocity characterizes the ultimate instability with respect to vortex nucleation. The relation between the critical velocity v_{cb} and the core size a was first discussed in Ref. 24 in the context of a continuous vortex in ^{3}He-A. For ^{4}He-II with a of atomic size, $v_{cb} \sim v_{cL}$, i.e. it is on the order of the Landau limit for the emission of rotons. In the case of ^{3}He-B, v_{cb} is close to the Landau critical velocity for the creation of quasi particle excitations, $v_{cL} = \Delta/p_F = 0.235\, \hbar/m\xi$ which follows from Eq.(1). In ^{3}He-B

a rigorous calculation can be performed to find the exact maximum value for the superfluid current and its corresponding velocity in homogeneous superflow. The velocity has a temperature and pressure dependence which somewhat resembles that of the superfluid energy gap Δ and in the limit $T \to 0$ approaches the Landau value $v_{cL} = \Delta/p_F$.

In ^{4}He-II sufficiently high critical velocities, which could be associated with intrinsic vortex nucleation, have customarily only been observed in measurements of ion propagation.[9,25-27] At high ion velocities the additional damping has been interpreted as being due to the nucleation of vortex rings with a diameter comparable to the effective size of the ion itself, *i.e.* a few nm. In recent years new techniques for fabricating orifices of sub-micron size and the possibility to perform measurements with single vortex sensitivity have revealed remarkably lucid observations of periodic phase slip events.[21,22] When the flow driven through a submicron-size aperture reaches the critical value, a phase slip by 2π or its multiple occurs and is removed from the phase gradient between the input and output sides of the orifice. Thus the velocity in Eq. (2) and the hydrodynamic energy in the orifice flow are reduced by the equivalent number of circulation quanta. In an aperture of submicron size the phase slips occur at a critical velocity on the order of 10 m/s, which approaches the values measured for vortex ring production in ion propagation.

According to present interpretation, a phase slip in the orifice flow is started by a nucleation event. Initially a segment of a vortex ring is thought to appear at some asperity on the rim of the orifice. In the presence of finite dissipation, the loop expands and ultimately crosses all the stream lines emerging from the orifice. The motion across all stream lines constitutes the phase slip by 2π. At low temperatures when dissipation is weak, the vortex loop may travel a long distance with the flow before it crosses the stream lines. In this process the vortex is washed away from the orifice such that no remanent filaments are left behind in the orifice itself.

The phase slip measurements[21,22] have been interpreted in terms of a temperature-dependent sequence of three processes which facilitate the nucleation of a vortex ring of self-sustained radius (Fig. 2): (1) At higher temperatures, *thermal activation* gives rise to a temperature-dependent critical velocity $v_{cT} \approx v_0(1 - T/T_0)$, with $v_0 \sim 10$ m/s and $T_0 \sim 2.5$ K. (2) At $T_q \approx 0.15$ K, a cross-over to the regime of *quantum nucleation* takes place. Below T_q thermal activation is bypassed by tunneling across the nucleation barrier, with an attempt frequency $\omega_0 = k_B T_q/\hbar \approx 10^{10}$ Hz, which provides a temperature independent nucleation rate and critical velocity v_{cq}.[21,28] (3) Finally, at the lowest temperatures of the present experimental range, nucleation is enhanced by ^{3}He impurity atoms,[15] which are attracted to the orifice by the pressure difference created by the supercurrent. There ^{3}He

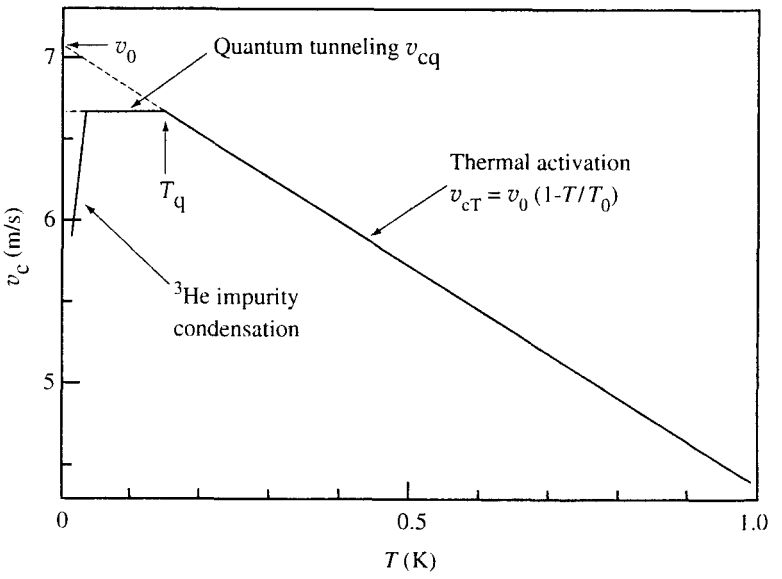

Fig. 2. Different temperature regimes of the intrinsic critical velocity in ^{4}He-II, based on measurements of superflow through a sub-micron-size orifice in Refs. 21 and 22.

atoms preferentially collect in the core of the nucleating vortex segment, where they have a bound state with a binding energy of ≈ 2 K. This reduces the barrier height in quantum nucleation and leads to a v_c which rapidly decreases with T.

The phase slip measurements in submicron orifices have been most important in clarifying the nature of dissipation in superflow, notably by demonstrating that the much lower critical velocities measured for wider channels require a different explanation. For this the rival alternative,[29] based on the motion of pre-existing vortex lines, provides now the accepted picture.

The second recent development, which has cast new light on the nature of critical velocities, are rotating experiments on the A and B phases of superfluid ^{3}He. These measurements have illuminated the problem from a different angle, namely via the influence of the vortex core radius a. The quasi-isotropic ^{3}He-B phase is expected to display hydrodynamic properties similar to those of ^{4}He-II. It has turned out that intrinsic nucleation of vortices can be observed in a mm-size rotating container filled with bulk ^{3}He-B superfluid. This difference from ^{4}He-II is attributed to the 2–3 orders of magnitude larger vortex core radius in ^{3}He-B. In fact, it is found that in a smooth-walled container remanent vortices are not left behind at all,

if the existing vortices are allowed to annihilate at the walls in zero flow conditions for a few minutes.

C. Outline of Contents

The reduced role of trapped vorticity and the absence of thermally activated vortex nucleation in superfluid ^{3}He offer a unique possibility to approach the bulk instability limit of superflow in a large container with bulk liquid. Inspired by this, we started studies of vortex formation in rotating ^{3}He-B.[30] These measurements are performed in the viscous temperature regime where dissipation is finite.

We use the NMR technique which has proven useful in the identification of different vortex structures in superfluid ^{3}He.[31,32] The sensitivity has been improved such that it is possible to perform measurements with single-quantum resolution.[33] We find that in ^{3}He-B, depending on the surface quality of the container, either extrinsic or intrinsic mechanisms of vortex formation dominate. They can be investigated in a rotating experiment as a function of the rotation velocity Ω, temperature T and pressure P by measuring the critical rotation velocity $\Omega_c(T, P)$ at which vortices are created. In linear flow measurements the critical value represents the transition from a dissipationless to a dissipative regime. In the rotating case it separates the two fundamentally different states of a superfluid in rotation: 1) vortex-free counterflow at low velocities, where the normal component corotates with the container while the superfluid component remains at rest with respect to the laboratory, and 2) the equilibrium state with rectilinear vortex lines, where the superfluid component also corotates, if viewed on a length scale larger than the inter-vortex distance.

Our results confirm the two expected differences between ^{4}He-II and ^{3}He-B, which result from the larger core size of the ^{3}He-B vortex: 1) weaker pinning and 2) absence of thermal activation and quantum tunneling in nucleation. In fact, these features, which depend on the vortex core radius, are seen in their right context when one compares them for the following sequence of three superfluids: ^{4}He-II, ^{3}He-B, and ^{3}He-A, for which the corresponding core radii a are approximately 0.1 nm, 10–100 nm, and 10–100 μm.

The most basic conclusions from our measurements on ^{3}He-B can be summarized in perhaps the following way: 1) The vortices are formed at the wall of the container by either extrinsic or intrinsic mechanisms. 2) In a sufficiently smooth-walled container only intrinsic nucleation is possible. 3) In this case the measured critical velocity $v_c(T, P)$ approaches the bulk superflow instability limit $v_{cb}(T, P)$, within a factor of 3 at best in our measurements, and is 3 orders of magnitude higher than the critical

velocity at which the first vortex becomes energetically stable in the rotating container and which is on the order of the Feynman velocity of Eq. (3). We find that v_c and v_{ch} are related via a scaling law which involves the vortex core size and a length l characterizing surface roughness at the nucleation site. This connection, we believe, is sufficient experimental proof that intrinsic nucleation in ^{3}He-B takes place at the superflow instability limit and that the validity of the order-of-magnitude relation $v_{ch} \sim h/m\xi$ is justified.

The contents of the paper are arranged as follows. Section II describes briefly the most important well-known theoretical aspects of vortex nucleation, superflow stability, vortex dynamics, and the structure of the vortex state in a rotating container. Section III describes how the NMR technique is used for monitoring vortex formation. Section IV reports measurements on single vortex nucleation. It demonstrates how extrinsic and intrinsic vortex formation manifest themselves and how they can be distinguished. Section V presents results on the measured intrinsic critical velocity, and describes how it is related to the bulk superflow instability in the presence of rough container surfaces.

II. THEORETICAL BACKGROUND

A. Nucleation Barrier and Critical Velocities

In this Section we focus on vortex nucleation in the ideal situation in a large rotating container at finite temperature. To describe the nucleation event consider the classic model of a small vortex half-ring (Fig. 1) interacting with the wall and the imposed superflow having the velocity $\mathbf{v}_s$.[3] The free energy of the loop corresponds to the energy needed to maintain it in a reversible manner with radius $\mathscr{R}$ in the externally applied superflow at the velocity $\mathbf{v}_s$. Finite dissipation at nonzero temperature preserves thermal equilibrium when the loop changes in radius and crosses stream lines. Initially its formation is thought to have been activated by the energy supplied from other excitation baths. This simple approach will not yield the actual dynamics of a nucleation event but it will give a reasonably correct nucleation barrier height.

Suppose therefore that a vortex half-ring of radius $\mathscr{R}$ (in the plane perpendicular to the wall) is attached to the wall at both ends (Fig. 1). Its flow field $\mathbf{v}_s^{(0)}$ in the presence of the wall coincides with the flow field of a complete ring with the same radius in homogeneous superflow with the velocity $\mathbf{v}_s$. The kinetic energy is

$$E_{kin} = \frac{1}{2} \int \rho_s (v_s^{(0)})^2 \, dV = \frac{\rho_s \kappa^2 L}{4\pi} \ln\left(\frac{\alpha \mathscr{R}}{a}\right) \tag{5}$$

Here $L = \pi\mathscr{R}$ is the length of the vortex loop. The factor α in the logarithm depends on the specific model of the vortex core: for a hollow core, for example, $\alpha = 8/e^2 = 1.08$.

The logarithmic approximation in Eq. (5) is valid in the limit $\mathscr{R}/a \gg 1$. When $\mathscr{R}$ decreases and approaches the core radius a, the logarithm transforms into some other function which depends on the actual core structure and in the limit $\mathscr{R} \to 0$ vanishes at least as rapidly as $\mathscr{R}^2$. The reason is that the total energy of the vortex loop vanishes at least as $\mathscr{R}^3$ when the vortex loop becomes smaller than a. We can interpolate between the two limits by writing

$$E_{kin} = \frac{\rho_s \kappa^2 \mathscr{R}}{4} \ln[\sqrt{(\alpha\mathscr{R}/a)^2 + 1}] \tag{6}$$

The momentum associated with the vortex loop along the x axis parallel to the wall and perpendicular to the plane of the loop is

$$p_x = \int \rho_s v_{sx}^{(0)}\, dV = -\kappa \rho_s S \tag{7}$$

where S is the area confined between the wall and the vortex loop, $S = \frac{1}{2}\pi\mathscr{R}^2$.

The total free energy, the work needed to create the vortex loop in the superflow field $\mathbf{v}_s$ in a reversible process, is given by

$$\mathscr{E} = E_{kin} + \mathbf{p}\mathbf{v}_s = \frac{\kappa\rho_s}{4}\left(\kappa\mathscr{R} \ln[\sqrt{(\alpha\mathscr{R}/a)^2 + 1}] - 2\pi\mathscr{R}^2 v_s\right) \tag{8}$$

The first term can be interpreted as the attraction to the wall, while the second attempts to inflate the vortex loop, to encompass more stream lines of the superflow. The energy $\mathscr{E}$ as a function of the loop radius $\mathscr{R}$ and the superflow velocity v_s is plotted in Fig. 3. For given v_s, $\mathscr{E}$ has a maximum at a radius which we denote $\mathscr{R}_0(v_s)$. The location of the maximum is defined by the largest root of the equation

$$v_s = \frac{\kappa}{4\pi\mathscr{R}_0}\left(\ln[\sqrt{\gamma(\mathscr{R}_0/\mathscr{R}_c)^2 + 1}] + \frac{\gamma(\mathscr{R}_0/\mathscr{R}_c)^2}{\gamma(\mathscr{R}_0/\mathscr{R}_c)^2 + 1}\right) \tag{9}$$

where we use $\gamma = (\alpha\mathscr{R}_c/a)^2$. The height of the maximum at $\mathscr{R}_0(v_s)$ is the free energy barrier for the creation of the vortex half-ring in homogeneous superflow with the velocity v_s:

$$\mathscr{E}_0 = U_0 f(\mathscr{R}_0/\mathscr{R}_c) \tag{10}$$

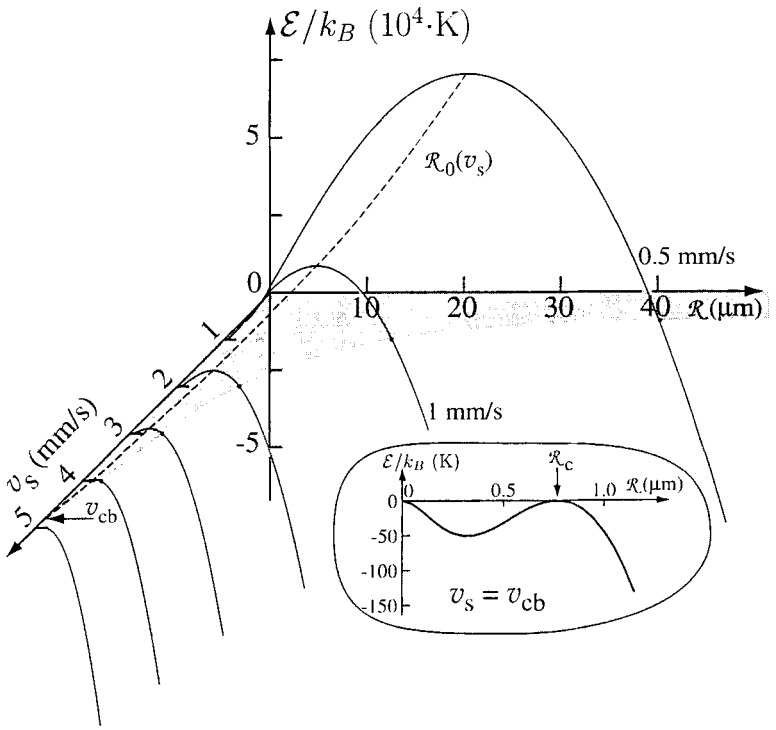

Fig. 3. Free energy of a vortex half-ring $\mathcal{E}$ (solid lines), plotted as a function of its radius $\mathcal{R}$ at different velocities v_s of the homogeneous externally driven superflow, according to Eq. (8). The shaded area marks the region in the $\mathcal{R}$ v_s plane where $\mathcal{E} > 0$. The location $\mathcal{R}_0(v_s)$ of the maximum, the nucleation barrier height $\mathcal{E}_0$ (dashed line), follows from Eq. (9). When $\mathcal{R}$ exceeds $\mathcal{R}_0$, the vortex expands spontaneously. The extrapolation $\mathcal{E}_0 \to 0$ defines v_{cb}. *Insert*: Eq. (8), when $v_s = v_{cb}$ and $\mathcal{E}_0 = 0$. This model is an approximate illustration of the nucleation energy $\mathcal{E}$ in the region of high v_s; accurate values of v_{cb} are plotted in Fig. 4. Values for ^{3}He-B at zero pressure have been used: $a \approx 5\xi(T, P)$ and $\xi(T = 0.75\, T_c, P = 0) = 84$ nm. With increasing pressure ξ and $\mathcal{E}_0$ decrease, but v_{cb} increases.

where

$$f(x) = x\left(\ln[\sqrt{\gamma x^2 + 1}] - \frac{\gamma x^2}{\gamma x^2 + 1}\right) \tag{11}$$

Here it is now convenient to define the parameter $\mathcal{R}_c$ in Eqs. (9), (10) as the critical radius at which the barrier height $\mathcal{E}_0$ ultimately vanishes at sufficiently high velocity v_s, *i.e.* where $\mathcal{R}_c = \mathcal{R}_0(v_s)$ and $v_s = v_{cb}$. This happens when $f(1) = 0$, which gives the root $\gamma \approx 3.92$ and

$$\mathcal{R}_c \approx 1.98a/\alpha \tag{12}$$

The characteristic scale of the free energy barrier is

$$U_0 = \tfrac{1}{8}\kappa^2 \rho_s \mathscr{R}_c = \beta \kappa^2 \rho_s a \tag{13}$$

where $\beta = 1.98/8\alpha$ is a model-dependent factor of order unity. For the hollow vortex core $\beta \approx 0.23$. In order of magnitude, U_0 is 4 K for ^{4}He-II and $2 \cdot 10^3$ K for ^{3}He-B at $T = P = 0$.

Equation (9) defines the radius of the loop while it is in unstable equilibrium under the action of two opposing forces: the contraction from the line tension and the expansion from the superflow field at v_s. In the presence of dissipation, a loop with radius larger than $\mathscr{R}_0$ will expand while a smaller one will shrink away. In increasing flow, Eq. (9) defines the threshold velocity from where the loop starts to expand across the flow. During its expansion the vortex reduces the flow velocity by the equivalent of a 2π phase slip. Note that, if the flow is reversed, *i.e.* v_s in Eq. (8) changes sign, the energy of the vortex half-ring becomes a monotonically decreasing function of $\mathscr{R}$: the loop in the reversed flow shrinks and annihilates without energy barrier at the lateral container wall.[34, 35]

In principle, these considerations also apply to a closed vortex ring in bulk superfluid,[18, 19] the only difference being a two times higher energy barrier with $L = 2\pi\mathscr{R}$ and $S = \pi\mathscr{R}^2$. Similar to the situation at the wall, also in the bulk it is the normal component which provides the frame with respect to which v_s is measured. In practice, the maximum velocity and minimum barrier height is generally reached at the outer wall of the rotating container, at some sharp wedge-shaped asperity which becomes the nucleation center. Therefore, experimentally one measures an average velocity for the critical flow which is less than the actual value at the asperity (Sec. II C 2).

The energy barrier determined by Eq. (10) vanishes when $\mathscr{R}_0(v_s) = \mathscr{R}_c$. Together with Eq. (9), which gives the location of the maximum of the energy barrier, we obtain the critical velocity

$$v_{cb} = \frac{\kappa}{2\pi\mathscr{R}_c} \frac{\gamma}{\gamma + 1} \tag{14}$$

At this *intrinsic instability velocity* bulk superflow becomes unstable with respect to the spontaneous formation of a vortex loop at the wall and the spontaneous reduction of the phase gradient of the order parameter. The intrinsic limiting velocity $v_{cb} \sim \kappa/2\pi a$ is the highest possible velocity at which homogeneous superflow can be sustained. It is independent of the container, determined by the intrinsic properties of the superfluid. In ^{4}He-II with $a \approx 1.5$ Å it is close to the Landau limit determined by the roton gap

and momentum. In ^{3}He-B, a is on the order of 1000 Å and v_{cb} correspondingly three orders of magnitude smaller. In practice, the measured critical value represents the average flow and does depend on the container.

The nucleating vortex loop has the smallest possible radius which is on the order of the core radius a. In this limit Eq. (14) is a rough estimate, since Eq. (6) for the kinetic energy in the range $\mathscr{R} \sim a$ is a crude simplification. Therefore, as can already be guessed from Eq. (14), the true stability limit v_{cb} can only be found by solving the specific stability problem with the proper structure of the superfluid order parameter. It is calculated by finding the maximum of the supercurrent j_s as a function of its velocity v_s. The criterion $dj_s/dv_s > 0$ is equivalent to the condition that the free energy functional of homogeneous flow has a minimum: its variation has only positive eigenvalues. Beyond this limit, homogeneous superflow cannot exist and an instability develops which tends to reduce v_s. The outcome from the instability should then be an object which has nonzero velocity circulation around itself and the smallest possible energy. This is nothing but a vortex. It may appear either at the wall in a form of a vortex loop or in bulk as a closed vortex ring. It can survive in the flow at v_{cb} only if it continuously expands and crosses the streamlines thereby dissipating the flow energy. Its inflation either reduces the superflow or resists some external drive which tends to increase v_s.

Microscopic calculations of the bulk critical velocity have been performed in Refs. 36 for ^{3}He-B. More recent calculations[37] of v_{cb}, using the scheme outlined in Refs. 36 but with updated Fermi-liquid parameters,[38] are shown in Fig. 4. In the Ginzburg–Landau regime, this velocity can be expressed in closed form,

$$v_{cb}(T) = 1.61(1 + \tfrac{1}{3}F_1^s)\sqrt{1 - T/T_c}\; k_B T_c/p_F \tag{15}$$

where F_1^s is the Fermi liquid parameter. In order of magnitude the energy of the superflow at the velocity v_{cb} equals the condensation energy. Since the coherence length ξ is determined through the condition that the gradient energy of order parameter variations on the scale of ξ is equal to the condensation energy, we again obtain the estimate in Eq. (4) for v_{cb}. For this reason, with $a \sim \xi$, the bulk superflow instability limit v_{cb} becomes comparable in magnitude to the Landau critical velocity, which in ^{3}He-B represents the spontaneous breaking of Cooper pairs and the emission of quasiparticle excitations. However, v_{cb} may also be associated with the Landau critical velocity for vortex-loop excitations at the wall where the energy and momentum of the loop are determined by Eqs. (5) and (7). Which of these two events will take place on reaching the instability may depend on the experimental set-up: In the case of the vibrating wire

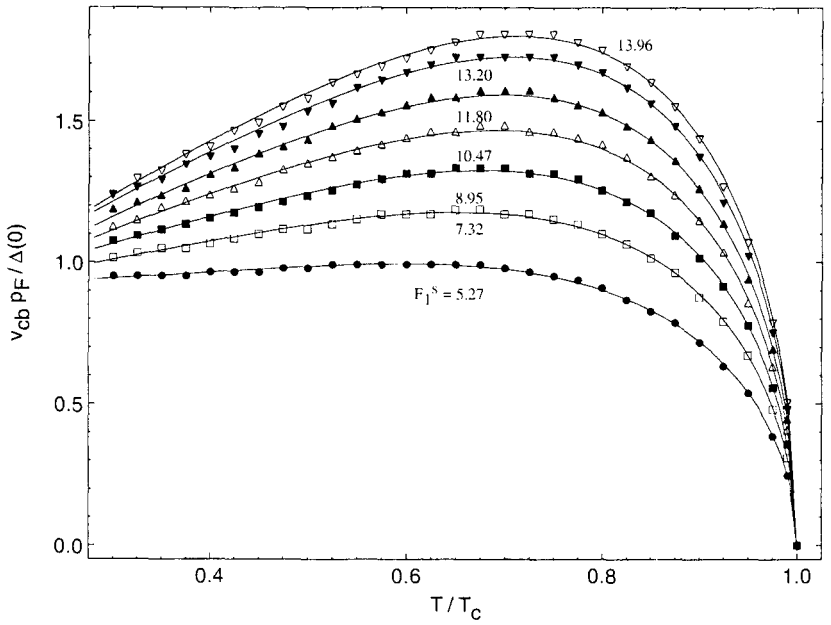

Fig. 4. Calculated intrinsic critical velocity v_{cb} of the bulk superflow instability in ^{3}He-B, as a function of normalized temperature T/T_c. The normalized value $v_{cb}\, p_F/\Delta(0)$ has been plotted. It converges to 1, when $T \to 0$. In this limit $v_{cb} = v_{cL}$. The scaling factor $\Delta(0)/p_F$ is 2.7 cm/s at zero pressure and increases to 6.5 cm/s at melting pressure (34.4 bar). The remaining dependence of the curves on pressure is via the Fermi liquid parameter F_1^s (which increases from 5.4 to 14.6 in the same pressure interval[38]).

viscometer it appears to be the former[12] while in the rotating container it is the latter.

B. Thermal Activation and Quantum Tunneling

At subcritical velocities $v_s < v_{cb}$, vortices can be nucleated in superflow via thermal activation over or quantum tunneling across the energy barrier. The probability of a nucleation event activated by thermal fluctuations with an attempt frequency ω_0 is given by

$$\Gamma = \omega_0 \exp(-\mathscr{E}_0/k_B T) \tag{16}$$

Since in ^{4}He-II $U_0 \approx 4\,\mathrm{K}$ and the temperatures are $T \lesssim T_\lambda \approx 2\,\mathrm{K}$, one expects that thermal nucleation of a vortex loop with a length of several a should be possible even for v_s well below v_{cb}.

In practice, the onset of nucleation can be observed above a certain threshold rate Γ_0 which depends on the sensitivity of the measuring set-up as a function of the externally applied superflow velocity v_s. The threshold rate determines the constant ratio $\mathscr{E}_0/k_B T = A$, which thus cannot be too large; A depends on the attempt frequency ω_0: $A = \ln(\omega_0/\Gamma_0)$. Since the energy barrier is a decreasing function of v_s, the onset velocity will increase and approach v_{cb} as the temperature decreases. This can be seen from simple arguments as follows[21]: Consider the vicinity of the critical velocity v_{cb}. One can here approximately write Eq. (10) in the form

$$\mathscr{E}_0 \approx \frac{2\gamma U_0}{\gamma + 1}\left(1 - \frac{v_s}{v_{cb}}\right) \tag{17}$$

The onset velocity for thermally activated nucleation, with the detection threshold defined from $\mathscr{E}_0 = Ak_B T$, becomes

$$v_{cT} = v_{cb}\left[1 - \frac{(\gamma + 1)\, Ak_B T}{2\gamma U_0}\right] \tag{18}$$

For ^{4}He-II, the slope of v_{cT} as a function of T is quite observable, as can be seen from the results in Refs. (21) and (22) and Fig. 2, which illustrates schematically the measured temperature dependence. From the theoretical model discussed above, one would expect the measurements to extrapolate to $v_{cT}(T \to 0) = v_0 = v_{cb}$, but the measured extrapolation is approximately $v_0 \approx 0.1\, v_{cb}$ (Fig. 2). The reason for this is not clear; one possibility is the effect of surface roughness, as discussed in Sec. IIC2.

Below a characteristic temperature $T_q \sim \hbar\omega_0/k_B$, quantum tunneling of vortices through the energy barrier in Eq. (10) bypasses the thermally activated process and becomes the dominant nucleation mechanism.[39] The critical velocity v_{cq} is then temperature independent, and is determined by Eq. (18) with $T = T_q$. Experiments show that, below about 0.15 K the measured v_c saturates to a temperature-independent value, which is smaller than v_{cb} by some factor $\lesssim 10$, and which in Refs. 21 and 22 has been interpreted as quantum tunneling. This behavior is expected to characterize nucleation in the $T \to 0$ limit. However, experimentally it is found that at the lowest temperatures condensation of ^{3}He impurity atoms in the vortex core decreases the energy barrier and reduces the critical velocity.

In contrast, in ^{3}He-B we have

$$U_0/k_B T_c \sim E_F^2/(k_B T_c)^2 \sim 10^5 \tag{19}$$

since $E_F/k_B \sim 1$ K. Here we write $\kappa^2 \rho_s = 2p_F E_F/3\hbar$ when T is not too close to T_c. In the immediate vicinity of T_c, the barrier height decreases as

$\sqrt{1-T/T_c}$ since it is proportional to the product of $\rho_s \propto 1-T/T_c$ and $\xi \propto 1/\sqrt{1-T/T_c}$. The large exponent in Eq. (16) makes the probability of thermal nucleation prohibitively small for any v_s below v_{ch} even in any experimentally reasonable vicinity of T_c. In other words, the second term in Eq. (18) is negligible for a large energy barrier such as Eq. (19). Quantum tunneling through the energy barrier depends on the exponent $(E_F/k_B T_q)^2$, with $T_q < T_c$. Therefore, its probability is also negligible until $v_s = v_{ch}$. A reduction in the barrier height U_0 due to the condensation of impurity atoms in the nucleating vortex core is also out of question: Superfluid ^{3}He is inherently devoid of dissolved foreign impurities. Although critical velocity measurements with the present techniques are possible as close to T_c as $1-T/T_c \approx 10^{-3}$, thermal and quantum fluctuations can be expected to produce vortices in ^{3}He-B only when v_s is practically equal to v_{ch}.

C. Stability of Superflow at the Wall

Let us now assume that in ^{3}He-B the nucleation of a vortex takes place when the superflow reaches its intrinsic instability at v_{ch}. In the rotating container the maximum superflow velocity is achieved at the perimeter, at the cylindrical wall. How is the nucleation process affected by the presence of the container wall?

A wall can influence the superflow in two ways. First, its very presence may cause depairing and suppress the order-parameter field at distances from the wall which are comparable to the superfluid coherence length ξ. This fact may in principle change the conditions for the stability of the flow near the wall. The extent to which the order parameter is modified is determined by the amount of small-scale roughness, asperities of height $l \ll \xi$, which change quasiparticle scattering at the wall from specular towards diffusive. Second, a wall may also have large scale roughness with $l \gg \xi$ which modifies directly the flow pattern and the velocity distribution. To find the true critical velocity one has to solve the stability problem of superflow with the specific boundary conditions at a given surface profile. Evidently this cannot be done in the general case and therefore we shall next review some theoretical results, which have been obtained for a few simple cases.

1. Small-Scale Surface Roughness

Consider first a flat wall with given scattering characteristics for quasiparticles, which may range from specular to diffusive. The effect from the modification of the order-parameter at the wall on the stability of the superflow has been studied within a simple Ginzburg–Landau (GL) model for a one-component order parameter.[40] In superflow along the wall with

the velocity $v_s = (\hbar/m\xi)\, q$, the order parameter for homogeneous flow becomes $\exp(iqx/\xi)\, \psi(y)$, where x is the distance parallel to the flow and y perpendicular from the wall, and

$$\psi(y) = \Delta \sqrt{1-q^2} \tanh\left[\sqrt{\frac{1-q^2}{2}}\left(\frac{y}{\xi}+\gamma\right)\right] \tag{20}$$

The degree of diffuse scattering is described by the parameter γ: for $\gamma = \infty$ the order parameter remains unchanged at the wall (specular limit), while $\gamma = 0$ corresponds to complete pair breaking at the wall (diffuse limit). This approach is an oversimplification for ^{3}He-B since its multi-component structure and all the internal degrees of freedom are neglected.

The stability of the solution in Eq. (20) against small perturbations of ψ was studied both analytically and numerically for the most interesting case, when $\gamma = 0$ and the order parameter vanishes at the wall. The exact result is that this does not change the stability limit of superflow: it is determined by $q_c = 1/\sqrt{3}$, as in bulk liquid.

2. *Large-Scale Surface Roughness*

For the effect of large-scale surface roughness, let us next consider potential flow around some specific asperity on the wall, following Vinen.[41] At a distance $y > \xi$ from the defect the superflow is potential, the velocity potential being the phase of the order parameter. The defect disturbs the flow pattern and causes a local enhancement in the flow velocity. Within the potential flow model there is no mechanism which could cause an instability to appear. We simply assume that the stability is lost when the maximum local velocity exceeds the bulk stability limit v_{cb}. Originally in the case of ^{4}He-II Vinen assumed that the increase in the local flow velocity makes it possible to form a vortex loop of radius b, for which one otherwise would require a velocity on the order of $(\kappa/b)\ln(b/a)$ in the absence of the asperity. The mechanism, by which this loop is created, was not specified. For ^{3}He-B, the critical radius of the loop is simply $b \sim a$, according to the general relation Eq. (4).

Let us consider as an example 2-dimensional flow around an obstacle which has triangular shape with height l (Fig. 5). Close to the apex ($r \ll l$), the flow velocity along the surface is[42] $v \sim v_s (r/l)^{n-1}$, where $n = \pi/\alpha$. Here α is the outer apex angle and r is the distance from the apex. Far from the asperity, $r \gtrsim l$, the flow restores its homogeneous velocity $v \sim v_s$. For $\alpha > \pi$ the local velocity diverges as $r \to 0$. In the case of a superfluid a short-distance cut off, on the order of the vortex core size a, has to be imposed: at a distance from the apex which is on the order of $r \sim a$ the maximum possible velocity is limited to v_{cb}. If $l \gg a$, this requirement gives an estimate

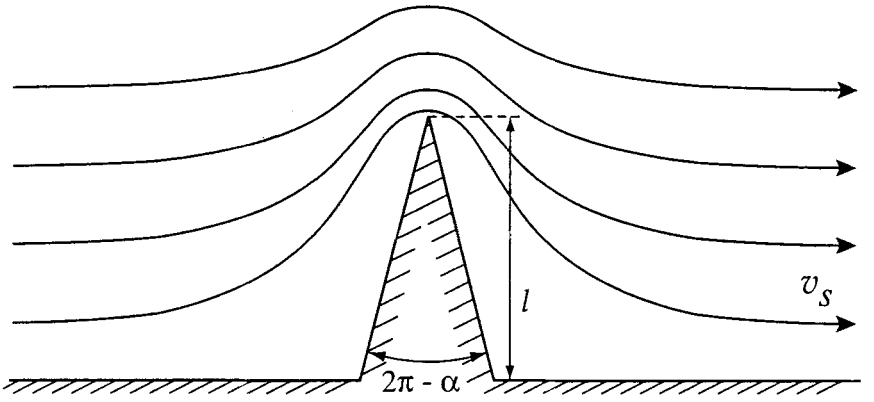

Fig. 5. 2-dimensional velocity field of superflow around a wedge-shaped "knife edge" on a flat wall.

for the critical average superflow velocity v_c which is needed to reach v_{cb} at the asperity

$$v_c = v_{cb}(a/l)^{\chi} \tag{21}$$

where $\chi = 1 - n$.

The reduction of the critical velocity from v_{cb} can thus be by a larger factor which has power-law dependence on the dimensions of the defect. A similar result can be obtained by considering a defect in the form of a step of height $l \gg a$. The reduction factors in all such cases seem to originate from the presence of a singular line on the surface, with a radius of curvature on the order of a or less. The largest effect is expected for a sharp protruding "knife edge" with $\alpha = 2\pi$ and $\chi = 1/2$, as suggested by Vinen.[41] In fact, Eq. (21) would predict that an arbitrarily large velocity enhancement can be achieved with a large enough value of l. In practice, there must exist a limit to this, caused by additional length scales, such as the structure of the defect along the third dimension: one expects that this models works better for more extended defects. Despite all its limitations, this model shows that the effect of large-scale surface roughness on the critical flow velocity can be appreciable. Note that cylindrical or spherical surface defects are less effective, since they are associated with a size-independent reduction factor of 2 or $\frac{3}{2}$, respectively.

This simple analysis can be compared with results from a numerical solution of the 2-dimensional GL equation of the model described in Sec. II C 1.[40] The GL equation was solved for a flow channel with a surface defect in the form of a rectangular bar (Fig. 6). It had a width w (along x)

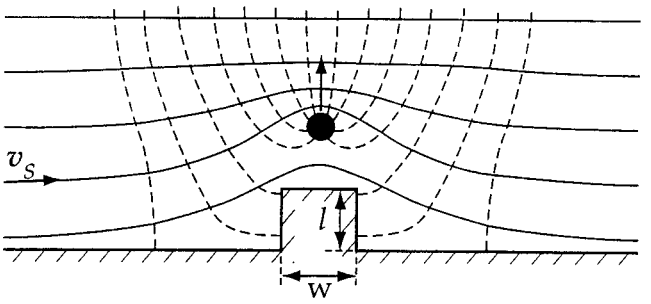

Fig. 6. Surface asperity with rectangular cross section in 2-dimensional superflow. When the superflow velocity is increased to $v_{c0}(\xi/l)^{\chi}$ at the entrance to the channel, the maximum velocity at the protrusion reaches the instability limit v_{c0}. A vortex (shown in cross section) is then nucleated at the protrusion. It moves in the direction of the arrow. Solid lines denote streamlines while the perpendicular dashed lines represent schematically the equiphasal contours. The latter have been drawn at $\pi/4$ phase intervals and their sum adds up to 2π on circling once around the vortex.

and height l (along y). The order parameter was required to vanish everywhere at the wall, including the surface defect. The numerical solution was worked out for the case when the flow velocity has a fixed value far from the defect. It was found that there exists a critical height l_c such that the solution of the GL equation for $l > l_c$ is topologically inequivalent to that for $l < l_c$: the order-parameter field contains a singularity with 2π-circulation of the phase around it, as shown in Fig. 6. This identifies the outcome from the instability as the nucleation of a single-quantum vortex. After the vortex is formed it moves away from the bump into the bulk superfluid and disappears at infinity under the action of the Magnus force produced by the flow. Note that the thermodynamic Ginzburg–Landau theory implies large dissipation which is needed to maintain thermal equilibrium. Within this model vortex motion is purely dissipative (i.e. no reactive part is present) and the newly formed vortex crosses all streamlines in the direction shown in Fig. 6. Thereby the phase difference between the inlet and outlet of the channel relaxes by 2π and the superflow velocity v_s decreases by $\Delta v_s = \kappa/L$, where L is the length of the channel.

We might note that for the values of l and w considered, v_c and the corresponding height l, at which the instability occurs, seem to be related by a power law as in Eq. (21) with $\chi = 0.36$, 0.33, and 0.29 for $w/\xi = 1$, 2, and 4, respectively (note that here $a \sim \xi$). The potential flow model also predicts an exponent χ which depends on the shape of the defect, but which is larger than what is obtained from the solution of the GL equations.[40] Indeed, a "knife edge" with an apex angle $\alpha = 2\pi$ is modelled by a wedge

with very small width. The potential model predicts $\chi = 1/2$, while the numerical calculations give $\chi = 0.36$ for $w/\xi = 1$. One more example is the case with $\alpha = \pi/2$ which corresponds to a blunt wedge. We have $\chi = 1/3$ and $\chi < 0.29$, for the potential flow model and numerical solution,[40] respectively. This implies that a 2-dimensional system described by the GL equation loses its stability at velocities which are higher than those predicted by the simple potential flow model. One reason might be that distortions in the order-parameter amplitude near sharp corners effectively smoothen their edges.

In practice it seems unlikely that real surfaces have roughness that can be considered to give rise to strictly 2-dimensional flow with the largest enhancement factors. We might expect that experimentally velocity enhancement is realistic by up to one, but not several orders in magnitude.

D. Rotating Superfluid

1. Lower Critical Rotation Velocity Ω_{c1}

When a cylindrical container filled with superfluid is slowly accelerated to rotation the vortex-free counterflow state is first established at low velocities. Here the normal component is clamped to corotation with the container while the superfluid component stays at rest with respect to the laboratory (we consider only rotation at constant Ω). In the rotating coordinate system the counterflow velocity is $\mathbf{v} = \mathbf{v}_s - \mathbf{v}_n = -\boldsymbol{\Omega} \times \mathbf{r}$. In contrast, the equilibrium state of the rotating superfluid is reached with a constant vortex density $n = 2\Omega/\kappa$. This situation mimics solid-body rotation on length scales larger than the intervortex distance r_v and is characterized by $\nabla \times \langle \mathbf{v}_s \rangle = 2\boldsymbol{\Omega}$.

In the rotating container there exists a lower critical rotation velocity Ω_{c1} at which it becomes energetically favorable to have the first vortex in the container. In the rotating frame, the energy of the liquid with one vortex in the center of a cylindrical container with radius R is

$$E = \frac{\rho_s}{2} \int (\mathbf{v}_s - \boldsymbol{\Omega} \times \mathbf{r})^2 \, d^2r$$

$$= \frac{\rho_s}{2} \int (\boldsymbol{\Omega} \times \mathbf{r})^2 \, d^2r + \frac{\kappa^2 \rho_s}{4\pi} \left[\ln\left(\frac{R}{a}\right) - \frac{2\pi\Omega R^2}{\kappa} \right] \tag{22}$$

The energy E becomes less than the energy of irrotational superflow in the pure counterflow state when $\Omega > \Omega_{c1}$, where

$$\Omega_{c1} = \frac{\kappa}{2\pi R^2} \ln \frac{R}{a} \tag{23}$$

The azimuthal counterflow velocity at the perimeter of the container, $\Omega_{c1} R$, is approximately two times larger than the Feynman critical velocity in Eq. (3) for linear flow in a tube of the same radius. In practice what happens at the lower critical rotation velocity Ω_{c1} depends on whether a source of vorticity exists in the container or not. If there are remanent vortices trapped on the wall, they will be released at velocities $\geqslant \Omega_{c1} R$, depending on the radius of the trapped vortex loop. If no extrinsic source of vorticity exists, then the first vortex will be nucleated at the upper critical velocity $\Omega_c \gg \Omega_{c1}$.

The first rotating experiments with ^{4}He-II and single-vortex resolution were performed by Packard and Sanders in the late nineteen sixties.[43] They found that the number of vortices was not too far from equilibrium at any given rotation velocity Ω. A new vortex seemed to appear whenever Ω was increased by an increment $\Delta\Omega$ which was on the order of Ω_{c1}. This indicates that vortices existed in surface traps on the wall of the container.

2. *Rotating States with Rectilinear Vortex Lines*

The equilibrium state in rotation consists of a central vortex cluster with rectilinear vortex lines which are isolated by a narrow annular vortex-free layer from the cylindrical side wall of the container (Fig. 7). This was first noted by Hall,[44] who calculated the total free energy $F = E_s - L_s \Omega$ in the rotating state by considering the kinetic energy E_s and the angular momentum L_s of the superfluid component. There are 3 contributions: 1) the energy of vortex lines, 2) the average solid-body-like rotation in the region with vortex lines, and 3) the counterflow in the outer vortex-free region. Minimization of the free energy yields for the width of the annular vortex-free region

$$D = r_c (\ln \sqrt{r_c/a})^{1/2} \tag{24}$$

where $r_c = \sqrt{\kappa/(2\pi\Omega)}$ is the radius of the Wigner-Seitz cell of the vortex lattice. The equilibrium number of vortices is then written as

$$N_c q = \pi (R - D)^2 (2\Omega/\kappa) = N_0 (1 - \sqrt{\Omega^*/\Omega})^2 \tag{25}$$

where $N_0 = \pi R^2 (2\Omega/\kappa)$ is the number of vortices in the continuum limit in the absence of a vortex-free region and $\Omega^* = (\kappa/4\pi R^2) \ln(r_c/a)$ is a measure of the relative width of the vortex-free region. The width D of the vortex-free region has been measured in the equilibrium vortex state in ^{3}He-B as a function of Ω in Refs. 45, 46, and 35. The result is in agreement with the value expected from Eq. (24). In the range of the present measurements

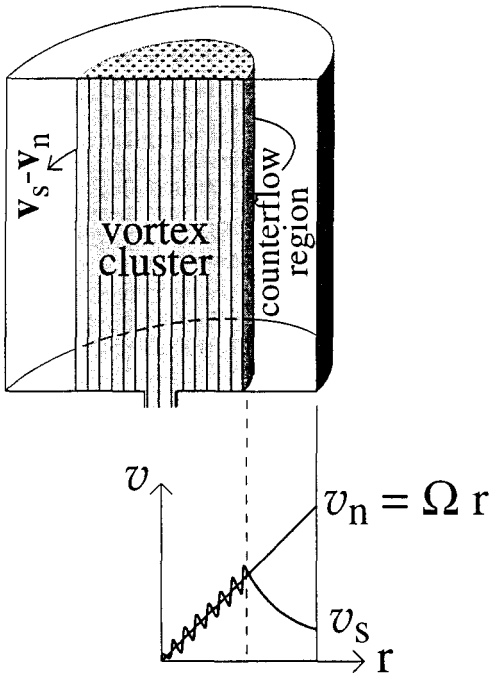

Fig. 7. Rectilinear quantized vortex lines in a rotating cylindrical container. In the metastable vortex cluster state the number of vortices is less than in the equilibrium state and the lines are constrained within a central cluster around which vortex-free counterflow circulates. The graph below the container shows the radial distributions of v_n and v_s. Inside the vortex cluster the average counterflow velocity $\mathbf{v} = \langle \mathbf{v}_s \rangle - \mathbf{v}_n$ vanishes while outside it is given by Eq. (27).

$\Omega^* \simeq 10^{-3}$ rad/s, which means that if, for simplicity, we set its value to zero, the error is less than 10%.

In ^{3}He-B, metastable states with less than the equilibrium number of vortices can be easily created since the upper critical rotation velocity Ω_c is typically 2–3 orders in magnitude larger than Ω_{c1}. These states consist of a central cluster of vortices surrounded by a vortex-free layer, as illustrated by the radial distributions of v_s and v_n in the lower part of Fig. 7. For later use, let us consider as an example how a vortex cluster with a preselected number of vortex lines is formed. The container is first rapidly accelerated to some $\Omega > \Omega_c$, whereby an unspecified number of vortices is created. These coalesce to a cluster of rectilinear vortex lines in the center of the container. Next, the number of vortices can be limited to any desired value

by decelerating to $\Omega = \Omega_v$, which forces the excess vortices to annihilate at the cylinder wall. The number of vortex lines thus obtained is $N = \pi R^2(2\Omega_v^*/\kappa)$, where

$$\Omega_v^* = \Omega_v(1 - \sqrt{\Omega^*/\Omega_v})^2 \tag{26}$$

is the "effective rotation velocity", corrected for the vortex-free layer of the equilibrium state. Here we assume that no annihilation barrier exists and the vortex state during deceleration, when vortices annihilate, adjusts itself to the equilibrium state appropriate to the instantaneous rotation velocity.[34,45,35] The cluster consisting of N vortices can thereafter be investigated at any velocity Ω in the interval $\Omega_v \leqslant \Omega \leqslant \Omega_v^* + \Omega_c$, i.e. Ω can be increased from Ω_v up to the critical value $\Omega_v^* + \Omega_c$, before new vortices start to appear. In this interval of rotation velocities, the radius R_v of the cluster is defined from the condition $N = \pi R_v^2(2\Omega/\kappa)$, which means $R_v = R\sqrt{\Omega_v^*/\Omega}$. Outside the cluster the azimuthal counter flow velocity is given by

$$|v| = \Omega r - N\kappa/(2\pi r) \tag{27}$$

Here the second term is the contribution from the central vortex cluster, which behaves like a giant vortex with the circulation $N\kappa$ and a surrounding superflow field decaying as $1/r$. The maximum counterflow velocity is at the cylinder wall:

$$|v| = R(\Omega - \Omega_v^*) \tag{28}$$

Experimentally there are two ways of producing an equilibrium state in rotating ^{3}He-B: 1) If the container is slowly cooled through T_c at constant Ω then the rotating superfluid will settle down in the minimum energy state. This procedure works in zero magnetic field at pressures below the polycritical point ($P \leqslant 21$ bar), when the A phase does not intervene between the normal and B phases. With a transition first to the A phase and only then into B phase, the situation becomes more complicated and may not lead to the equilibrium B phase state at all.[47] 2) A more practical way of producing the equilibrium state is to decelerate from a situation with a large number of vortices to some velocity Ω_v. The excess vortices are annihilated on the cylindrical wall during the deceleration and the final state at Ω_v then corresponds to one with the maximum possible number of vortices. Our measurements[35] indicate that above a cross-over velocity, which is typically of order 0.2 rad/s, the annihilation barrier vanishes and the maximum possible number of vortices at a given Ω equals the equilibrium number.

Nucleation and annihilation in the rotating container are not mirror processes of the same phenomenon. In a rotating cylinder, an annihilation barrier appears due to the vortex-free region near the container wall, if the axis of the cylinder is perfectly parallel with the rotation axis and its corners have a radius of curvature $\ll r_v$. In this case the outermost rectilinear vortex lines will not be able to cross spontaneously the annular vortex-free region which separates them from the cylindrical wall. By deceleration the number of vortex lines can then be increased above that of the equilibrium state. A misalignment of the lateral wall with respect to the rotation axis removes the annihilation barrier, since the outermost vortex lines become now curved and may attach to the side wall. Here they can slide in a continuous manner along the lateral wall and the maximum vortex number during deceleration will equal that in the equilibrium state.[34,35]

E. Vortex Pinning

A vortex may be trapped in a metastable energy minimum between two protrusions on the wall. This way it shortens its length and lowers its energy. A finite flow velocity v_{cp} is required to make it mobile. Suppose that a vortex loop is pinned between two asperities separated by a distance d from each other. As the flow increases, the loop bends more and more. The shortest radius of curvature which this trap can support is $d/2$. Equation (9) with $\mathscr{R}_0 = d/2$ determines the highest flow velocity which the pinned vortex can sustain.[16] This critical velocity does not depend on the characteristics of the pinning site; its origin is the same as for the Feynman velocity where the geometrical factor is taken to be the separation between the asperities. A more detailed analysis, performed by Schwarz,[48] gives

$$v_{cp} = \frac{\kappa}{2\pi d} \ln\left(\frac{b}{a}\right) \tag{29}$$

where b is the radius of the pinning asperity. The depinning velocity defined by Eq. (29) contains only a weak logarithmic dependence on the vortex core size. One should note, however, that Eq. (29) is valid for asperities with radii $b \gg a$; irregularities of the size $b \ll a$ would not be felt by a vortex. This suggests that a vortex with a smaller core size sees more pinning sites than one with a larger core. Thus pinning of vortices in ^{3}He superfluids would be less important than in ^{4}He-II.

A trapped vortex loop may be randomly oriented with respect to the flow. This introduces an additional $\cos\theta$ in Eq. (29): $v_{cp} = (\kappa/2\pi\, d \cos\theta) \ln(b/a)$ where θ is the angle between the flow and the normal to the plane of the loop.

F. Vortex Dynamics

A vortex nucleated at the container wall moves towards the center under the action of the Magnus force in the presence of damping provided by the mutual friction. The Magnus force $\mathbf{F}_M$ is oriented in the direction perpendicular to both the vortex core and the azimuthal counterflow. In the simple case of a fully stretched rectilinear vortex line $\|\Omega\|\hat{\mathbf{z}}$, the force $\mathbf{F}_M$ is given by

$$\mathbf{F}_M = \kappa\rho_s[\hat{\mathbf{z}} \times (\mathbf{v}_L - \mathbf{v}_s)] \tag{30}$$

Here $\mathbf{v}_L$ is the velocity of the vortex line and $\mathbf{v}_s$ is the local value of the superfluid velocity field, which in the general case derives contributions from both the macroscopic counterflow and from the presence of other vortices.

The mutual friction force arises from the motion of the vortex with respect to the normal component of the superfluid and can be parametrized in the form

$$\mathbf{F}_N = -D\mathbf{v}_L - D'[\hat{\mathbf{z}} \times \mathbf{v}_L] \tag{31}$$

where we have assumed that in the rotating container $v_n = 0$. The mutual friction parameters D and D' were originally[3] introduced in terms of the phenomenological Hall–Vinen coefficients B and B'

$$\frac{\rho_n}{2\rho} B = \frac{D/\kappa\rho_s}{(D/\kappa\rho_s)^2 + (1 - D'/\kappa\rho_s)^2} \tag{32}$$

$$\frac{\rho_n}{2\rho} B' - 1 = \frac{D'/\kappa\rho_s - 1}{(D/\kappa\rho_s)^2 + (1 - D'/\kappa\rho_s)^2} \tag{33}$$

The balance of the Magnus and mutual friction forces (in the transverse plane) gives the vortex line velocity

$$\mathbf{v}_L = \left(1 - B'\frac{\rho_n}{2\rho}\right)\mathbf{v}_s - B\frac{\rho_n}{2\rho}[\hat{\mathbf{z}} \times \mathbf{v}_s] \tag{34}$$

The velocity of the vortex $\mathbf{v}_L$ has thus both a large azimuthal component along $\mathbf{v}_s$ and an inward oriented radial component, proportional to the dissipative mutual friction. Often the friction force is expressed in terms of $\mathbf{v}_s$, instead of $\mathbf{v}_L$,

$$\mathbf{F}_N = \frac{\kappa\rho_s\rho_n}{2\rho}\{B\mathbf{v}_s - B'[\hat{\mathbf{z}} \times \mathbf{v}_s]\} \tag{35}$$

It includes a dissipative part oriented along $\mathbf{v}_s$ and are active part acting at a right angle to $\mathbf{v}_s$. The coefficients B and B' for ^{3}He-B were calculated in Refs. 49, 50 and measured in Ref. 51. The dissipative coefficient $B\rho_n/\rho$ is of order unity at about 0.5 T_c. It decreases rapidly when $T \to 0$ while towards increasing temperature it increases and diverges as $T \to T_c$.

In the absence of pinning a vortex half-ring, which has nucleated on the side wall, slides azimuthally and expands radially. It transforms into a straight vortex line when it meets the top and bottom surfaces of the cylinder. A fully extended rectilinear vortex moves on a spiral trajectory towards the center of the cell. Its distance r from the cylinder axis varies as $r = R \exp(-t\Omega B\rho_n/2\rho)$. The transit time is[45]

$$\Delta t = (\Omega B\rho_n/2\rho)^{-1} \ln(R/R_r) \tag{36}$$

where R_r is the radius of the central vortex cluster (Sec. II D). The transit time $\Delta t \sim 1$ s for $\Omega \sim 1$ rad/s. The motion of the vortex line is the slowest process in a nucleation or annihilation event, the bottle-neck, which sets the time resolution of our measurements. The transit time increases towards low temperatures because of the decreasing mutual friction parameter B.[49, 51]

G. Summary on Theoretical Background

At finite temperature, superflow becomes dissipative when a vortex starts moving. This transition is experimentally measured as a critical velocity which depends on the mechanism responsible for generating the mobile vortex. A hierarchy of different critical velocities exists: those based on extrinsic sources of vorticity are lower while intrinsic velocities for nucleating a new vortex are higher. Depending on the superfluid, measuring geometry, surface characteristics, choice of external variables, etc. one or more critical velocities are encountered in a given experiment. A summary of the various critical velocities can be found in Table I.

Below we list our main expectations on vortex formation in a rotating measurement on ^{3}He-B:

1. In a rotating cylinder vortex formation takes place at the cylindrical wall where the counterflow velocity reaches its maximum value at any given rotation velocity Ω.
2. Remanent vortices are less important in ^{3}He-B than in ^{4}He-II owing to a 10^2–10^3 times larger vortex core radius. Trapping and proliferation of pre-existing vortices is less prominent. The

TABLE I

Critical Velocity for Forming the First Vortex in Bulk Liquid ^{4}He-II or ^{3}He-B, in Order of Increasing Magnitude

Critical velocity	Definition	Phenomenon	Criterion	Observation
v_{cF}	Eq. (3)	Flow in tube	Minimum energy	Trapped vortices become mobile
v_{cA}	Eq. (23)	Vortex favorable in rotating container	Minimum energy	—"—
v_{cp}	Eq. (29)	Depinning of vortices	Minimum energy	—"—
v_{cT}, v_{cq}	Eq. (18)	Onset of thermal or quantum nucleation (^{4}He-II)	High probability of fluctuations	Orifice flow, ion propagation
v_{cL}	Eq. (1)	Pair breaking (^{3}He-B) or emission of rotons (^{4}He-II)	Single-particle excitation energy	Ion propagation, vibrating wire
v_{cb}	Eqs. (4), (15)	Barrier-free vortex formation (^{3}He-B)	Intrinsic instability of superflow	Vortex nucleation in rotation

measured critical velocity in a rotating container is more likely to exceed the low values typical of geometry dependent Feynman velocities.

3. The nucleation barrier is exceedingly high and the probability of nucleating an initial vortex half-ring by thermal or quantum fluctuations is zero at any practical temperature or superflow velocity below the superflow instability $v_{cb}(T, P)$. A nucleation event is expected to become possible only when the maximum local velocity of the vortex-free counterflow reaches the intrinsic v_{cb} of homogeneous bulk superflow.
4. The measured critical velocity will be affected by surface asperities on a length scale $l \gg \xi$. The signature from this reduction is expected to be revealed by a power law behavior: $v_c = v_{cb}(a/l)^{\chi}$ with $\chi \leqslant 1/2$. With a particularly smooth container surface one might expect that much higher relative values v_c/v_{cb} can be achieved than in ^{4}He-II.

III. EXPERIMENTAL TECHNIQUE

A. ^{3}He Sample Containers

Our critical velocity measurements have been performed in a rotating nuclear demagnetization cryostat. By monitoring the cw NMR signal we measure the number of vortex lines which are formed as a function of Ω. The NMR line shape is recorded at a fixed frequency ν by sweeping the steady polarization field H with a triangular linear ramp. The field is oriented along the rotation axis ($\mathbf{H} \| \Omega$). Low fields from 10 to 30 mT have been used, corresponding to the frequencies 0.3–1 MHz. This interval of fields is chosen for the following reasons. For measurements close to T_c, good frequency resolution is required for which a low field of 10 to 20 mT is recommended. The low fields are not useful at low temperatures due to poor resolution in the measurement of the absorption amplitude and, what is worse, due to the fact that the magnetic healing length of the B phase texture becomes too large compared to the container radius.[30] Therefore, 20–30 mT fields were employed for covering the low temperature range. The measured critical flow properties are not magnetic field dependent at these low fields.

The ^{3}He NMR cell is a cylindrical container with radius R and height L (Fig. 8). It is mounted on top of a long tube, or tower, with its symmetry axis $\hat{\mathbf{z}} \| \Omega \| \mathbf{H}$. The cylinder is separated from the ^{3}He tower by means of a small orifice. The orifice, usually 0.5 mm in diameter, provides the thermal

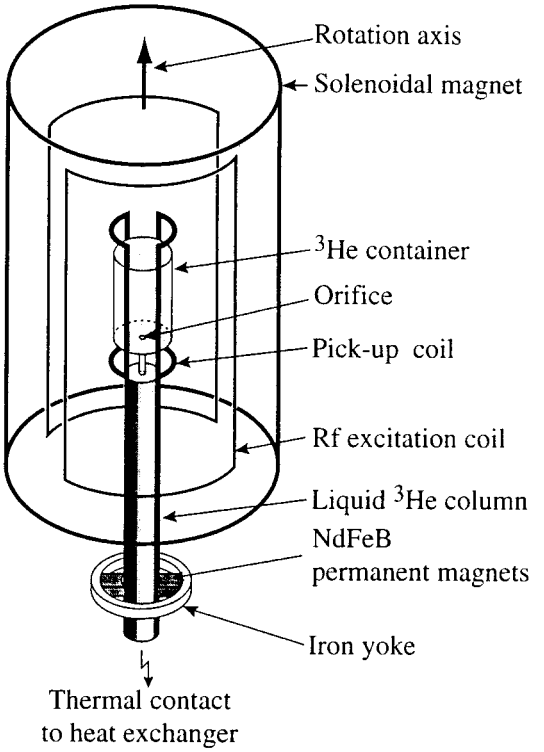

Fig. 8. ^{3}He tower with sample container and NMR coils. The cylindrical NMR cell is connected via a 60 mm long liquid ^{3}He column to a large ^{3}He volume with a sintered heat exchanger for thermal contact to the copper nuclear refrigeration stage, located below the parts shown here. A system of superconducting orthogonal coils is used for NMR. The pick-up and rf excitation coils are saddle-shaped, generating fields along the x and y axes. The axially oriented steady field is produced with an end-compensated solenoid. The pick-up coil is fixed on an epoxy coil former which is thermalized to the copper body of the ^{3}He cell while the other coils are thermally and mechanically connected to the mixing chamber, situated above the parts shown here. The actual dimensions of the large outer coils are not drawn to scale. The entire ^{3}He cell with the NMR coils is inside a superconducting Nb shield, to avoid interference from the demagnetization field for cooling and temperature stabilization. This Nb jacket is on the heat shield which is fixed to the mixing chamber.

contact to the NMR cell and is located in the center of the bottom plate of the container. A small orifice is necessary in order to reduce the leakage of vortices into the NMR cell from the lower parts of the ^{3}He volume, where they are formed first due to a large diameter of 30 mm and a rough wall consisting of a porous sintered heat exchanger.

Four different sample containers have been used in the critical velocity measurements to test for the influence of different surface finishes. Container #1 was machined from Stycast 1266 epoxy with a diameter $2R =$ height $L = 7$ mm. During its assembly the inside walls were painted over with fresh fluid epoxy to provide a shiny surface finish. The surface tension of the wet epoxy causes the paint to even out surface porosity and to round the corners. After all measurements had been finished with this container, it was cut in two halves and inspected with an optical microscope. The large scale cut-off for the surface roughness was found to be $10\,\mu$m.

The second container #2, with $R = 2$ mm and $L = 6$ mm, had a very rough cylindrical side wall due to pot-holes up to $300\,\mu$m in depth. To enhance the measuring sensitivity, the saddle-shaped pick-up coil, which consists of 2 equal halves with 60 turns each, was molded into the cylindrical epoxy wall immediately around the ^{3}He sample.

The parts for the third container #3 were cast on mylar covered surfaces, which provided mirror luster to all walls. These surfaces were significantly smoother than the $10\,\mu$m roughness in container #1. However, on glueing the bottom plate to the cylindrical wall a groove of $\sim 30\,\mu$m width and depth was left around the entire circular perimeter along which the two surfaces meet. This container had $R = 2.5$ mm and $L = 7$ mm.

Finally, the fourth container #4 was fabricated from fused quartz and had the same dimensions as #3. The two flat bottom pieces were fused to the cylinder with an oxygen-acetylene torch which produced smoothly rounded corners. As the final step the container was carefully cleaned by rinsing with various acids and water and then sealed with a piece of filter paper. Before mounting in the cryostat it was screened for defects and spots with a microscope. From the optical inspection one can conclude that in a clean state its surface roughness is expected to be below $1\,\mu$m.

In containers #1 and 4 no remanent vortices were observed and their critical velocities were the highest. These are also the two containers which, based on the optical examination, have the smoothest walls. Surface roughness measurements were later conducted on these containers using a stylus scanner with a tip of $2\,\mu$m radius of curvature and a laser interferometer for read-out. For container #1 the maximum peak height from the median level was found to be $1.7\,\mu$m while the standard deviation from the mean

was 0.3 μm. For container #4 these values were 0.4 and 0.005 μm, respectively. A scan along a horizontal line with a 4 μm wide stylus is expected to reveal the sharp peaks from the mean but not narrow grooves or pits. However, in both cases the surfaces have solidified from a plastic state with a large surface tension and are not expected to have sharp indentations. Thus the numbers for the epoxy or the quartz surfaces did not change when scanned in a second test with a stylus of 9 μm width.

B. NMR Spectrometer

The vortex lines are counted by monitoring the cw NMR spectrum. To reach the single-vortex detection limit in a rotating cryostat (which floats on air bearings and therefore has somewhat unstable reference voltage levels) we use a superconducting pick-up coil, a high quality tuning capacitance, galvanically decoupled rf excitation, and a GaAs FET preamplifier operating at liquid helium temperatures inside the vacuum can of the cryostat.[52] This scheme provides a Q value of 2000 for the resonance tank circuit. The low impedance output from the preamplifier secures good decoupling from external interference to the long connection to room temperature, where a band-pass amplifier and a phase sensitive detector with digital output is used for read-out. The axially oriented polarizing field is generated with a superconducting solenoid, which is located inside the vacuum jacket and is fed by a 14 bit programmable current source.

The liquid-helium (LHe) temperature preamplifier[52] is shown in Fig. 9. The two MESFET devices (Sony 3SK166) are connected in cascode to enhance decoupling of input and output. A difficulty with high frequency GaAs channel devices is parasitic oscillation at microwave frequencies. To secure stable operation the quench resistor R3 (47 Ω) is connected in series with the input gate and the capacitor C7 (47 pF) limits the bandwidth of the amplifier to 1 MHz.

One advantage from cooling the MESFETs to LHe temperatures comes from the exponentially decreasing gate leakage current, which reduces the shot noise. Neglecting the capacitive coupling from gate to channel and dielectric losses (of the transistor packages and the printed circuit board), we get from the measured leakage current of 12 pA an input equivalent noise of 2 fA/$\sqrt{\text{Hz}}$. With a voltage noise of 1.3 nV/$\sqrt{\text{Hz}}$ this leads to a noise temperature of 100 mK at an optimum source resistance of 650 kΩ. This allows the use of a high Q tank circuit with high passive gain at the input. At a drain–source bias current of 9 mA the gain is $\approx$20 and the power consumption 80 mW. The circuit is built with surface-mount type components on a circuit board with an electrically (and thermally) grounded back plate to reduce stray inductance and capacitance. The wires are taken

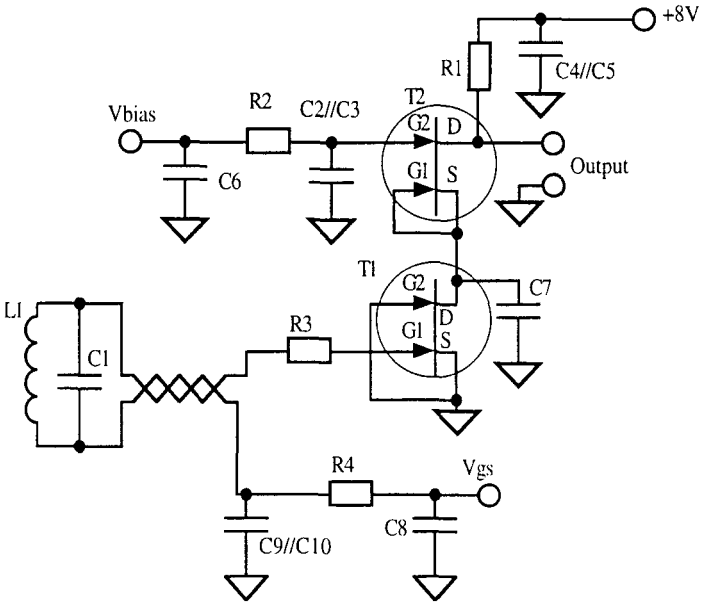

Fig. 9. GaAs MESFET preamplifier, which operates at 4 K with a high Q superconducting tank circuit (L1–C1).

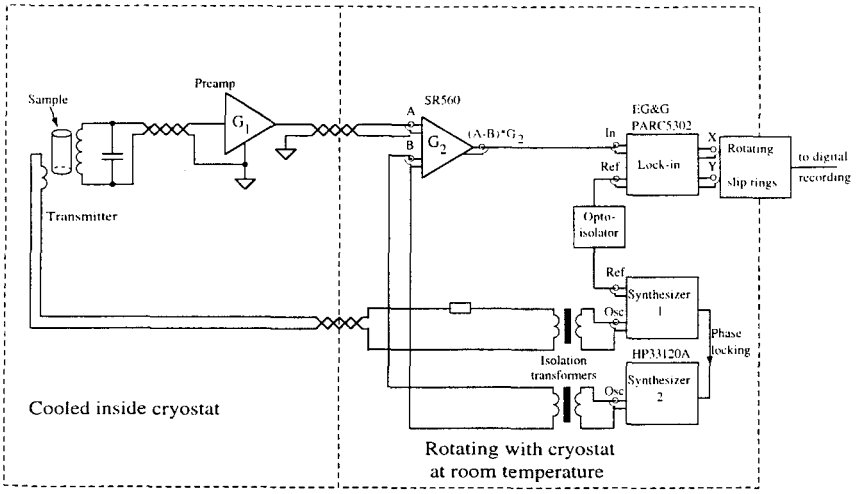

Fig. 10. Block diagram of the cw NMR spectrometer.

to the board as shielded twisted pairs. The 1/f noise limits the applicability of the MESFET transistors to above 100 kHz.

The block diagram of the spectrometer is shown in Fig. 10. The output from the LHe temperature preamplifier is fed to a differential band-pass amplifier. The second input of the differential amplifier is derived from a digital oscillator, which is phase-locked to an identical master oscillator. The master oscillator supplies the rf excitation while the phase and amplitude of the reference oscillator are adjusted to compensate the output of the differential amplifier to zero when the resonance excitation is switched on but the NMR field is off-resonance. The output device is a phase-sensitive detector which operates at the resonance frequency. Its phase is adjusted to give a symmetric Fermi liquid absorption signal with a smoothly continuous baseline.

C. NMR Line Shape

Examples of NMR spectra for 3 different rotational states are shown in Fig. 11. The line shapes in the nonrotating ($\Omega = 0$) and the equilibrium vortex ($\Omega_v = \Omega$) states are very similar. They are characteristic of the "flare-out" texture, which the B phase anisotropy vector $\hat{\mathbf{n}}$ forms in cylindrical geometry in an axially oriented polarizing field.[53] Here a large fraction of the absorption is piled against the Larmor edge at $\nu_0 = \gamma H$ and only a shallow tail extends to higher frequencies, with a cut-off at $\nu \approx \nu_0 + (\nu_L^2/2\nu_0)\sin^2\beta_c$, where β_c is close to the value $\arccos(1/\sqrt{5})$, the angle which $\hat{\mathbf{n}}$ would form with the surface in axial field at rest ($\Omega = 0$). Thus the cut-off frequency is $\nu \approx \nu_0 + 0.4\,\nu_L^2/\nu_0$. The absorption in this region originates from the liquid close to the cylindrical perimeter. In contrast, the peak bordering on the Larmor edge is produced by the liquid in the central region of the cylinder, where $\mathbf{n}$ is still largely oriented along $\mathbf{H}$. In the equilibrium vortex state, with no macroscopic counterflow, the NMR line shape remains roughly unchanged as a function of Ω (see, however, Ref. 54).

In the vortex-free counterflow state, in contrast, the large kinetic energy density (via the density anisotropy[55]) exerts a dominating orienting influence on the texture.[56] The absorption is then to a large extent shifted into a counterflow peak with a frequency shift which is close to the cut-off value of the $\Omega = 0$ state signal. The spectrum in a metastable vortex cluster state is a compromise between these two extremes.[30] The strong dependence of the line shape on the velocity of the macroscopic counterflow is the property which allows us to monitor the number of vortex lines up to single-vortex resolution.

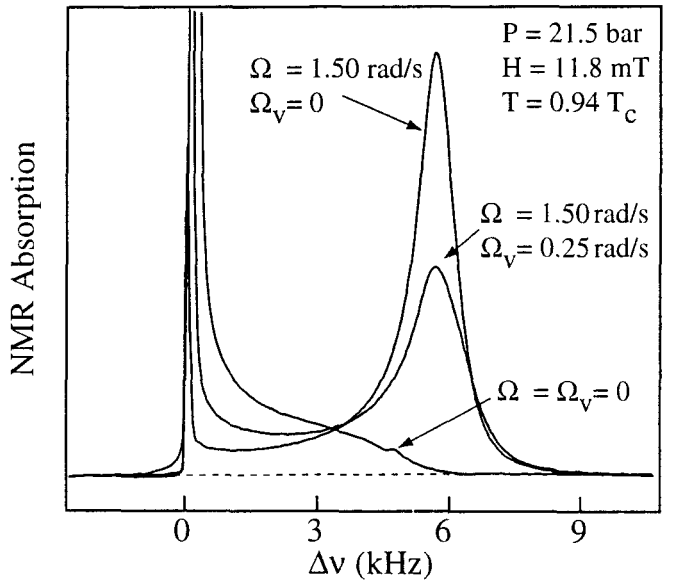

Fig. 11. NMR line shapes of three different rotational states as a function of the frequency shift $\Delta\nu = \nu - \nu_0$ from the Larmor frequency $\nu_0 = \gamma H$: a) nonrotating state, $\Omega = 0$, b) vortex cluster state at $\Omega = 1.5$ rad/s with $\Omega_v = 0.25$ rad/s, and c) vortex-free counterflow at $\Omega = 1.5$ rad/s. The equilibrium vortex state ($\Omega \approx \Omega_v$) is not distinguishable from the nonrotating state in the small scale presentation of this plot (cf. Fig. 12 in the region $\Omega < 0.3$ rad/s). The signals have been measured in container #4.

D. NMR Measuring Procedures

The simplest variation of the critical velocity measurement is to cool the sample at constant pressure P at rest ($\Omega = 0$) into the superfluid phase. When the temperature has been stabilized to the desired value T, then the cryostat is slowly accelerated to rotation. Generally a well-defined and reproducible critical angular rotation velocity $\Omega_c(T, P)$ can be identified during the constant acceleration. Beyond this point, vortex lines start to appear and form a cluster of rectilinear lines in the center of the container while the counterflow velocity remains limited to the critical value. If Ω is increased sufficiently slowly compared to the viscous relaxation times, then dynamic effects become unimportant during the acceleration.[45] Alternatively in scanning for the critical velocity, one can also keep Ω constant and sweep the temperature. During the sweep the NMR absorption is monitored continuously. It signals the point when the critical velocity is reached and vortex lines start forming.

The temperature in the sample volume can be determined by two different means from the NMR spectra. In principle the more accurate reading is provided by integrating the absorption under the complete resonance line. The result, when normalized to the absorption of the resonance signal measured in the normal Fermi liquid, is compared to the temperature dependence of the static susceptibility. It has been measured, *eg.* in Ref. 57, which we use here to provide the correspondence between the integrated normalized absorption and temperature. The precision in the measurement of the integrated absorption is characterized by a standard deviation of 0.3 for the Fermi liquid signal. On cooling below T_c the susceptibility decreases, the signal is broadened by frequency shifts, and although the rf excitation can be increased due to faster relaxation, nevertheless, the precision gradually decreases.

In practice a simpler technique is to measure the frequency shift of the large counterflow resonance peak, from which one obtains $v_L(T, P)$. Its temperature dependence, measured in Refs. 54 and 58, then provides the temperature reading. To reach the saturated frequency shift $\Delta\nu_{cf} \approx 0.4\nu_L^2/\nu_0$ of the counterflow resonance peak, a reasonably high counterflow velocity $\Omega - \Omega_c \gtrsim 1$ rad/s is recommended. The temperature is regulated by controlling the magnetic field on the nuclear refrigerant. In these measurements it can be kept constant with a precision of $\Delta T/T_c \simeq \pm(1...3) \cdot 10^{-3}$ by adjusting the demagnetization rate such that the frequency shift of the counterflow peak does not drift.

In a smooth-walled container the metastable vortex cluster state can reproducibly be formed with a fixed number of vortex lines. The high critical velocity allows dynamic measurements on the vortex array in the cluster using a time dependent rotation drive. In such a measurement the temporal response of the vortex array can be investigated at densities $n \neq 2\Omega/\kappa$, without interference from uncontrolled nucleation or annihilation of vortices, quite unlike the situation in rotating ^{4}He-II.

E. Vortex Line Count

The order parameter texture depends on the proportion of counterflow to vortices. This provides the means for monitoring the number of vortex lines in the rotating container. Suppose one records continuously the absorption level at fixed ν and H at the location of the Larmor peak, as shown in Fig. 12. With increasing Ω the signal first decreases, indicating an increasing counterflow velocity v, which deflects $\hat{\mathbf{n}}$ more and more from the axial orientation even in the central region of the cylinder. This trend is reversed beyond some critical counterflow velocity $v_c = \Omega_c R$, where distinct step-like increases in the absorption start to appear. Each of the steps

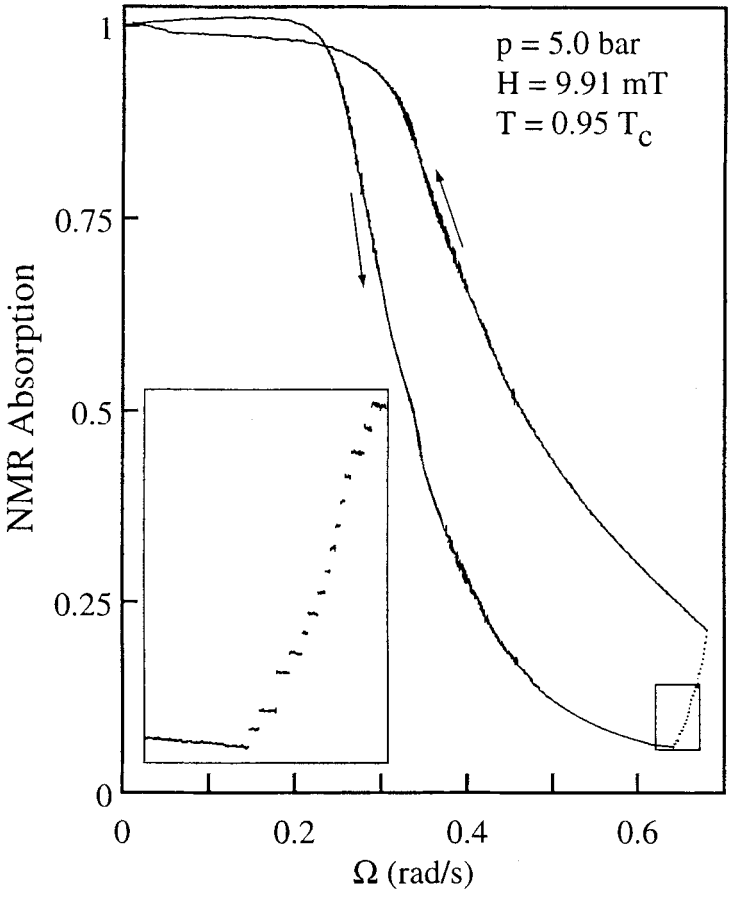

Fig. 12. The peak height of the absorption maximum in the Larmor region plotted as a function of Ω during an acceleration-deceleration cycle past the nucleation threshold. The vertical scale denotes the peak height normalized to its value in the nonrotating state. The insert displays a magnified view of the discontinuous step-like increase in absorption when periodic nucleation with increasing Ω sets in. Acceleration is reversed to deceleration at the upper end of the staircase pattern and the peak height starts to increase continuously with decreasing counterflow. At about 0.3 rad/s the counterflow has been reduced to zero, the peak height has almost regained its full value, and the existing vortices start annihilating during further deceleration. Container #3 has been used in this demonstration.

corresponds to an event in which one or more vortex lines are formed. These migrate to the center of the container, where the orienting effect of the counterflow is now reduced. Since the Larmor peak arises from the central part of the cylinder with axial $\hat{\mathbf{n}}$ orientation, each new vortex helps to restore its absorption and therefore appears as a step up.

During further acceleration more vortex lines are created and the vortex cluster in the center grows in radius. Different mechanisms may be responsible for the appearance of vortices, but in general beyond the first critical threshold the counterflow velocity v does not increase substantially during further acceleration, since more and more vortex lines will be generated.

When the acceleration is reversed to deceleration, the counterflow velocity first decreases and the vortex cluster expands. Here the Larmor peak continuously increases until its peak height has returned almost to the original level, as v approaches zero. At this point the cluster has expanded to the cylindrical wall of the container and vortex lines start to annihilate during further deceleration. The present measurement is not sensitive to annihilation and this process is not visible in Fig. 12; it can be studied with other techniques.[35,46]

In recent measurements the vortex line count has been performed with single vortex resolution[33] by counting steps as in Fig. 12. In the early measurements with container #1 the resolution was ± 10 vortices.[30] Even this sensitivity is sufficient to determine v_c since the number of vortices at the relevant angular velocities is large: In the equilibrium state their number is $N_{vq} \approx 2\pi R^2 \Omega/\kappa \approx 1200$ at $\Omega = 1$ rad/s (container #1). To measure Ω_c in a well-behaved case, *i.e.* to identify the threshold of intrinsic nucleation, one only needs to look for the discontinuity in the derivative of the absorption as a function of Ω in a record like that of Fig. 12, even if no separate steps are distinguishable. The change in slope can be detected by various NMR schemes. Coherent dynamic states are expected to be particularly useful for this purpose. The resonance mode known as the *homogeneously precessing domain* (HPD) has been partly used to collect the data in Figs. 19, 26 and 29 (see below), by employing the methods explained in Ref. 59.

Often it is desirable to determine the number of vortices in an unknown vortex cluster. This can be performed by bracketing Ω_c^* iteratively between two known values. These are obtained by sequentially reducing Ω to lower and lower values, until the outermost vortex lines in the expanding cluster start to annihilate and the NMR signal starts changing. In practice, the measuring process is performed at constant temperature, as depicted in Fig. 13, in the following way:

Suppose the cluster exists originally at some velocity Ω_i. First a suitable reference velocity Ω_r is chosen. For this an initial guess of Ω_c^* is made such that the difference $\Omega_r - \Omega_c^* \simeq 0.5...1$ rad/s and a fair size counterflow

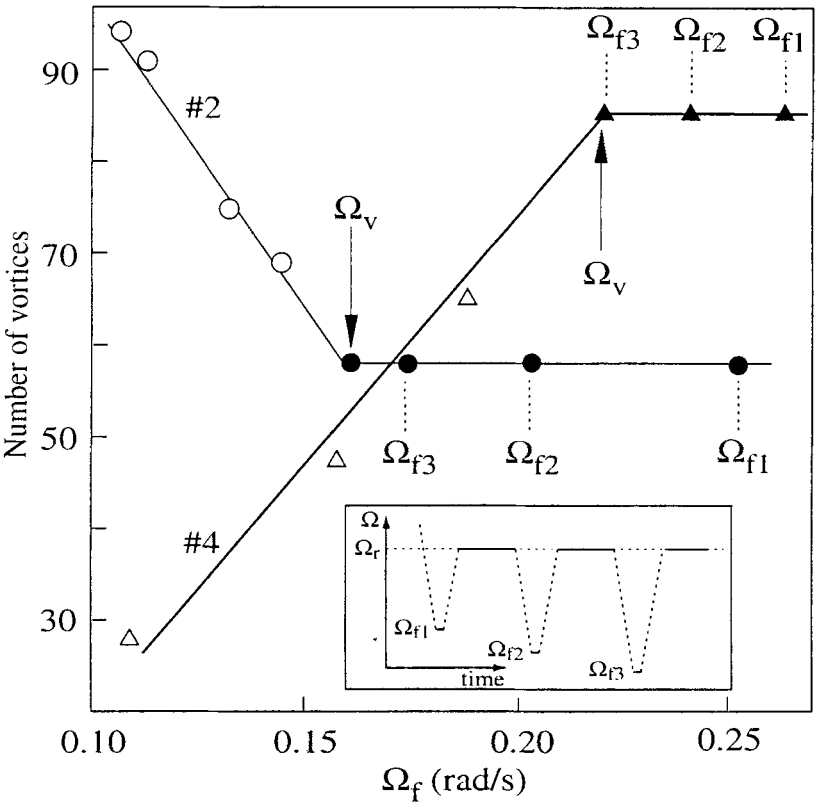

Fig. 13. Measuring procedure for determining the number of vortices in a vortex cluster of unknown size. In the *insert* is shown as a function of time the iterative sequence of deceleration steps to successively lower values of Ω_{fi}, to locate the value of Ω_r where the vortex cluster has expanded to the cylindrical wall. Above the insert the number of vortex lines is plotted as a function of Ω_f, as measured at the reference velocity Ω_r after each deceleration step to Ω_{fi}. When $\Omega_{fi} > \Omega_r$ the number of vortices in the cluster remains unchanged (filled data points), but once Ω_{fi} drops below Ω_r, vortices start to annihilate in container #4, where no remanent vortices are trapped (△). In container #2 pieces from the annihilating vortices are trapped on the cylindrical wall during deceleration; during acceleration from $\Omega_{fi} < \Omega_r$ to Ω_r they give rise to new vortices and the vortex number actually increases (○). In the latter case the initial state was created in the first acceleration past the nucleation threshold, so that no trapped vortices existed at the start of the measurement and the number of vortices remains constant during the acceleration from Ω_{fi} to Ω_r as long as $\Omega_{fi} > \Omega_r$ (●). The vertical scale has been obtained from calibration runs in which nucleation steps are counted as a function of the corresponding peak height ratio of the counterflow and Larmor maxima.

absoption peak is formed at Ω_r. The first reference spectrum is then measured at Ω_r. Next the rotation velocity is briefly reduced to some value Ω_{f1}, where it is kept for 1 min, and is then raised back to Ω_r. If the spectrum measured at Ω_r after the deceleration is unchanged from that before, then the vortex cluster did not yet expand to the wall and lose vortices. The deceleration is repeated to a lower value Ω_{f2}, such that the difference $\Omega_{f1}-\Omega_{f2}$ is the desired precision in the determination of the vortex number. Finally, if the process of deceleration is repeated n times to successively lower values Ω_{fn}, then the indication that $\Omega_{fn}<\Omega_t^*$ has been reached is the following: Until $\Omega_{f(n-1)}$ the line shape measured at Ω_r remains unchanged but from then on during further deceleration it starts to change. With some practice, this iterative determination can be performed with a precision $\Omega_{f(n-1)}-\Omega_{fn}<0.02$ rad/s, the decisive factor being the value of $\Omega_r-\Omega_t^*$, *i.e.* the sensitivity of the reference spectrum to a change in the vortex number. The method works well in the virgin state where there are no remanent vortices trapped on the walls of the container at the start of the calibration process.

It is the newly formed and fully expanded rectilinear vortex line in the central region of the container which gives rise to a step in the insert of Fig. 12. This means that only the last phase in the process, which leads to a new vortex line, is made visible by the response in the NMR absorption and that the dynamics of the absorption response is dominated by the time scale of vortex motion, the transit time determined by Eq. (36). The bottleneck is thus the mutual-friction-generated motion, which is slow compared to the nucleation (or annihilation) process at the side wall.

IV. NATURE OF CRITICAL VELOCITY

A. Measurement of Critical Velocity

Let us examine periodic nucleation of vortices during constant acceleration past the critical threshold in more detail, by inspecting Fig. 14. The isothermal acceleration is here performed slowly, such that the system remains in equilibrium, *i.e.* dynamic events occur on a time scale much faster than that determined by the rate of change of Ω. At Ω_c the counterflow velocity reaches the critical value $\mathbf{v}_c=-\boldsymbol{\Omega}_c\times\mathbf{R}$ for the first time and the first vortex loop is nucleated. Next, this segment of a vortex ring expands and in its final state it becomes a rectilinear vortex line in the center of the container, contributing a step increase to the absorption of the Larmor peak.

In the lower part of Fig. 14 the nucleation events have been replotted in a style familiar from linear flow measurements, namely the counterflow velocity $|v|$ as a function of the drive Ω. When the first vortex is nucleated

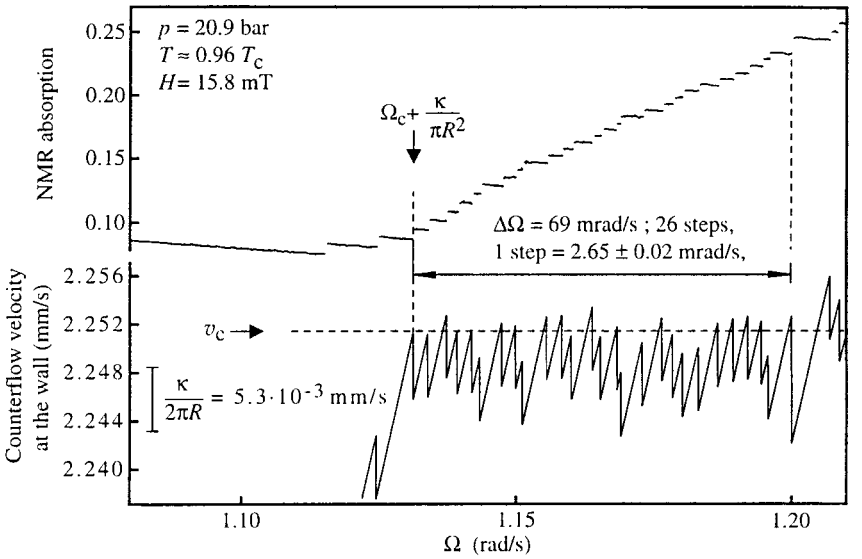

Fig. 14. Single-quantum nucleation: Nucleation of vortices as a function of Ω during acceleration ($d\Omega/dt = 2.4 \cdot 10^{-4}$ rad/s^2) in container #2. *Top*: The vertical axis denotes the height of the Larmor peak, normalized to its value in the nonrotating state. Vortex formation starts with the first step-like increase at 1.115 rad/s, but the nucleation threshold Ω_c is identified from the third step (dashed vertical line), where the critical flow velocity v_c reaches a stable value (dashed horizontal line). On the far right at 1.200 rad/s there is a step which corresponds to 2 circulation quanta. *Bottom*: The corresponding counterflow velocity $v = (\Omega - \Omega_c^*)\, R$ at the cylindrical wall, with a discontinuous reduction equivalent to one circulation quantum $\kappa = h/(2m_3) = 0.0662$ mm^2/s at each step.

the velocity at the side wall drops from $|v| = \Omega_c R$ by $\Delta v = \kappa/(2\pi R)$, *i.e.* by the equivalent of one circulation quantum. After the sudden drop, the velocity regains its increasing slope until the second step in the absorption signal, when v again discontinuously decreases to $|v| = \Omega R - \kappa/(\pi R)$. This behavior reflects the fact that nucleation is controlled by the maximum counterflow velocity $|v| = \Omega_c R$, which is not changing during the acceleration and is reached at the cylindrical wall.

The average of the maxima in the saw-tooth pattern in Fig. 14 defines the critical velocity $v_c = \Omega_c R$. Its standard deviation is roughly $\kappa/(4\pi R)$ or half of the equivalent of one circulation quantum. The horizontal distance of the single-phase-slip steps is ideally $\Delta\Omega = \kappa/(2\pi R^2) \approx 2.6 \cdot 10^{-3}$ rad/s for container #2. This agrees with the measurement, within a standard deviation of $\approx \frac{1}{2}\Delta\Omega$. The prime restriction to better precision is thought to arise from mechanical noise, which affects both the measuring accuracy of Ω and its stability. The overall standard deviation in Ω has been measured to be $\pm 1 \cdot 10^{-3}$ in the velocity range of Ω_c.. In addition there may exist a

contribution of more subtle origin to the noise in v_c, associated with the same features which give rise to nucleation events of multiple quanta.

A rerun of the measurement in Fig. 14 is shown in Fig. 15. It has been recorded in roughly the same conditions, but this time the steps are consistently double-quantum events. Out of some 20 measurements in very similar conditions only this one produced regularly double-quantum events. The most frequent case is not steps consistently with the same quantum number, but, as shown in Fig. 16, steps of varying multiplicity of the circulation quantum. Note that a high step, where several vortices are formed simultaneously, reduces the counterflow velocity substantially. It is followed by a long plateau, which is needed to build up the counterflow velocity back to the critical value. Thus multiple quantum steps broaden the width of the critical region.

Multiple quantum steps are more prominent at high pressure where the coherence length ξ is shorter. It is also believed that they are more frequent in the presence of a rough side wall, like in the case of container #2. This would suggest that here nucleation might be activated at several

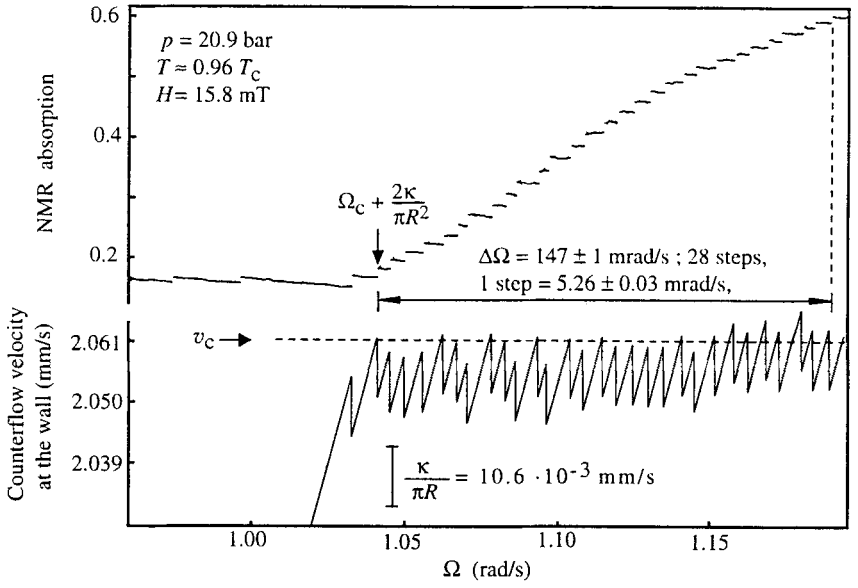

Fig. 15. Double-quantum nucleation: Periodic nucleation at constant acceleration, as in Fig. 14, but with all events giving rise to two vortices. Only the first two premature steps on the extreme left are single-quantum events (which suggests that they have a different origin from the later steps). Note the twice as large vertical scale of the counterflow velocity in this figure, compared to Fig. 14. The measurement has been performed in approximately the same conditions in container #2 as those in Figs. 14 and 16.

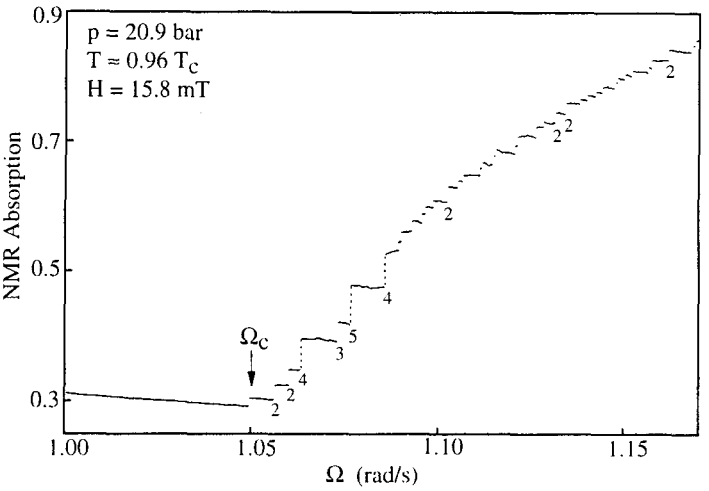

Fig. 16. Multiple-quantum nucleation: Periodic nucleation at constant acceleration, as in Fig. 14, often leads to events in which varying numbers of vortices appear to be nucleating simultaneously. The steps with multiple quanta are indicated by their appropriate number of quanta. Within the response time of the measurement, which here is fixed by the time constant of the lock-in amplifier to 0.1 s, the steps appear to be instantaneous.

competing sites within the span of the transit time given in Eq. (36), which it takes a vortex line to move to the center of the container, before the full effect is felt in the counterflow velocity (see Sec. IVC1). Another explanation, for consistent steps with double multiplicity, might be a special geometry of the nucleation site. If the nucleated vortex filament recurrently expands along a particular trajectory where it is cut into two pieces by an intersecting edge or protrusion, then one would regularly end up with two vortex lines.

We have not performed a systematic study of the quantum number of the nucleation events as a function of the externally controllable parameters, to find out whether only one vortex loop is originally nucleated or several at different sites simultaneously. A similar unsolved question is the cause for the premature steps in Figs. 14 and 15, where a few vortex lines are seen to appear before the counterflow velocity has reached its critical value.

B. Intrinsic Nucleation

Single-vortex resolution allows us to identify intrinsic nucleation: A periodic sequence of single-quantum steps as in Fig. 14, with a stable and reproducible value of v_c as a function of the drive Ω, distinguishes intrinsic

nucleation. Several additional features can be listed to illustrate the nature of intrinsic nucleation events.

The critical velocity Ω_c has a nonmonotonic temperature dependence (Fig. 19). The $\Omega_c(T, P)$ boundary may be traversed either isothermally in accelerating rotation, as was done in Figs. 14, 15, and 16, or isorotationally by sweeping T, the case in Fig. 17. In both instances one starts approaching the critical line from the counterflow state located below the $\Omega_c(T, P)$ curve and a staircase pattern is traced when the critical line is reached. In intrinsic nucleation the critical values do not depend on whether Ω or T is the scanned variable.

The nucleation threshold is governed by the counterflow velocity at the cylindrical wall and is independent of the number of vortex lines in the central cluster. This measurement is illustrated in Fig. 18, where Ω_c has been measured as a function of Ω_r, the experimental parameter which controls the number of vortices in the cluster. The result demonstrates that vortices

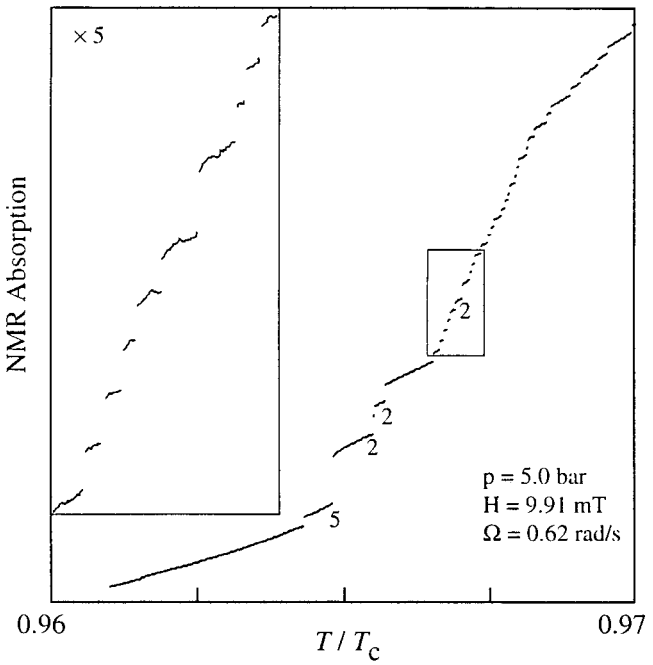

Fig. 17. Nucleation sequence during warm-up at constant $dT/dt = 0.26\,\mu$K/min and $\Omega = 0.62$ rad/s. The steps are of both single and multiple quantum size. The latter are identified by their appropriate number of quanta. The insert shows a five times magnified blow-up from the region within the rectangle. Container #3 has been used in this measurement.

start appearing in the NMR cell when the flow velocity at the side wall reaches the critical value $|v_c| = (\Omega - \Omega_c^*)\, R = \Omega_c R$, independently of Ω_v. We postpone the discussion on the results from Ω_c measurements until Sec. V.

In our rough-walled containers #2 and 3 a reproducible Ω_c can only be measured in the virgin state, when no prior annihilation of vortices has taken place. Once vortices have been annihilated in decelerating rotation, trapped remanent vorticity is always present to some degree. This will be discussed in the next section.

C. Extrinsic Mechanisms

We have identified three sources of extrinsic vortex formation in a closed rotating container: (1) The migration of vortices into the sample container during accelerating rotation from other parts of the ^{3}He volume,

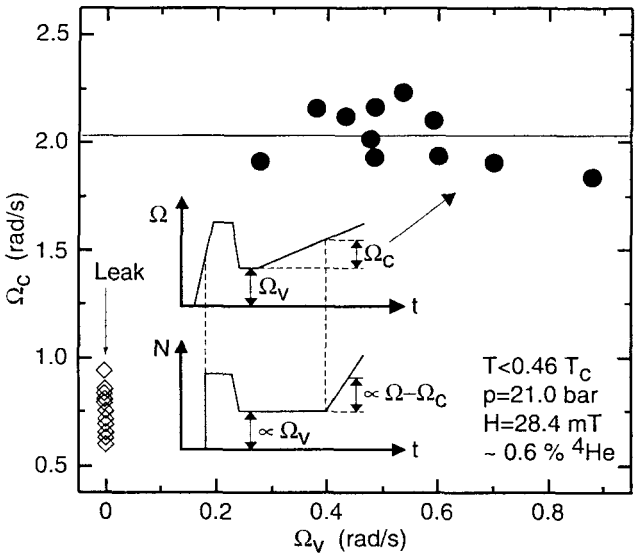

Fig. 18. Critical rotation velocity Ω_c as a function of the number of vortices $N \propto \Omega_v$, which form the initial vortex cluster: (●) Ω_c is independent of Ω_v, when measured in the presence of an initial vortex cluster blocking the orifice; (◇) in the absence of a cluster ($\Omega_v = 0$) the first vortices are formed in a sudden avalanche during accelerating rotation ($d\Omega/dt > 0$). The *insert* illustrates the measuring procedure as a function of time t: (*top*) the rotation drive Ω for forming the vortex cluster and the subsequent measurement of Ω_c, and (*bottom*) the number N of vortices in the container during these operations. The process for forming the initial cluster makes use of the burst-like formation of vortices. The measurements have been performed with container #1.

where they have been formed earlier. Remanent vortex filaments trapped on the walls of the container give rise to new vortices during accelerating rotation (2) at randomly varying counterflow velocities or (3) recurrently at a constant critical velocity. Let us consider these in turn.

1. Vortex Leakage

The prime source for vortex formation in vortex-free counterflow below 0.6 T_c in container #1 was found to be a sudden burst which instantaneously leads to a large cluster of vortex lines. This process is characterized by three features: 1) It is prominent in container #1, which has a large orifice of 1 mm in diameter. 2) It depends on $d\Omega/dt$: it is not observed at constant Ω, even in the presence of a temperature sweep. 3) If the orifice is covered with a vortex cluster to start with, then the possibility of burst-like vortex formation is greatly reduced. This technique made the measurements in Fig. 18 possible.

As shown in Fig. 19, burst-like vortex formation depends strongly on temperature. Below $T \simeq 0.5\ T_c$ it provides a second parallel branch of vortex formation at low superflow velocities. The branch with the higher critical velocity $v_c = \Omega_c(T, P)\ R$ corresponds to intrinsic nucleation. It can be measured by either traversing the critical curve horizontally, *i.e.* by sweeping temperature at constant Ω, or vertically in isothermal conditions and accelerating rotation, but with a cluster of vortices covering the orifice.

An experiment in Fig. 20 illustrates how burst-like vortex formation is triggered by accelerating rotation. Here vortex-free counterflow is cooled at a constant rotation velocity of 1.4 rad/s to $T = 0.46\ T_c$, which brings the ^{3}He-B sample into the region between the two branches in Fig. 19, but in the vortex-free state. One period of a sine wave with an amplitude $\Delta\Omega = 0.1$ rad/s is then superimposed on the rotation drive. At this point the container is instantaneously flooded with a cluster such that the counterflow is reduced to $\Omega - \Omega_c < 0.3$ rad/s.

We attribute the burst-like vortex formation to the migration of vorticity through the orifice in the presence of sufficiently fast and accelerating counterflow. At constant Ω vortices below the orifice are stationary and are not observed to leak into the sample chamber. Acceleration forces the vortex lines below the orifice into motion, in an attempt to increase their density and restore the equilibrium value $n = 2\Omega/\kappa$. This triggers a sudden leakage through the orifice. If a vortex cluster already exists in the sample cell, then uncontrolled vortex motion is reduced during acceleration, because there is no counterflow near the orifice, and the risk of more vortices leaking into the container is minimized.

The phenomenon is an example of nonlinear avalanche behavior which is well-known from superconductors. In accelerating rotation, vortex

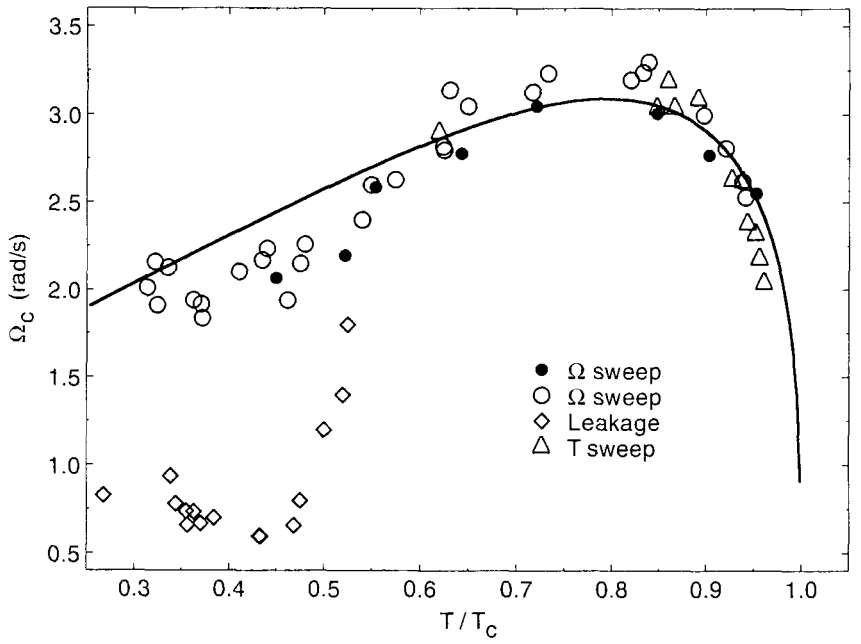

Fig. 19. Critical rotation velocity $\Omega_c(T)$ as a function of normalized temperature at 21 bar pressure. The nominal ^{4}He impurity content is 0.6% for most of the data (open symbols) but measurements with pure ^{3}He (●) show no distinguishable difference. Most data points (○, ●, ◇) have been measured by accelerating Ω at constant T but some (△) have also been recorded by sweeping T at constant Ω. The lower branch (◇) represents burst-like vortex formation through the central orifice in isothermal accelerating rotation, with no initial vortex cluster. The upper branch (○, ●) in this temperature region has been measured with an initial vortex cluster covering the orifice. The solid curve represents the same fit to Eq. (38) as in Fig. 26. Container #1 has been used.

lines which are below the orifice pinned to its rim, are forced into motion on a spiral trajectory towards the center. Mutual friction B decreases rapidly with temperature[51] and slows down the radial dissipative motion of vortex lines, as seen from Eq. (36). At sufficiently low temperatures the unpinned vortex will not have enough time to move out of the way and to reduce the counterflow substantially before other vortices also become unpinned. Thus a number of factors seem to promote the tendency towards turbulent vortex flow: 1) the unstable balance of the innermost vortices at the edge of the orifice, 2) the inhomogenous distribution of counterflow and vorticity in the orifice, 3) small viscous damping at low temperatures, and 4) sufficiently high counterflow velocity.

Similar factors might contribute to the multiple quantum nucleation events, which were discussed in Sec. IV A. Multiple quantum phase slips are

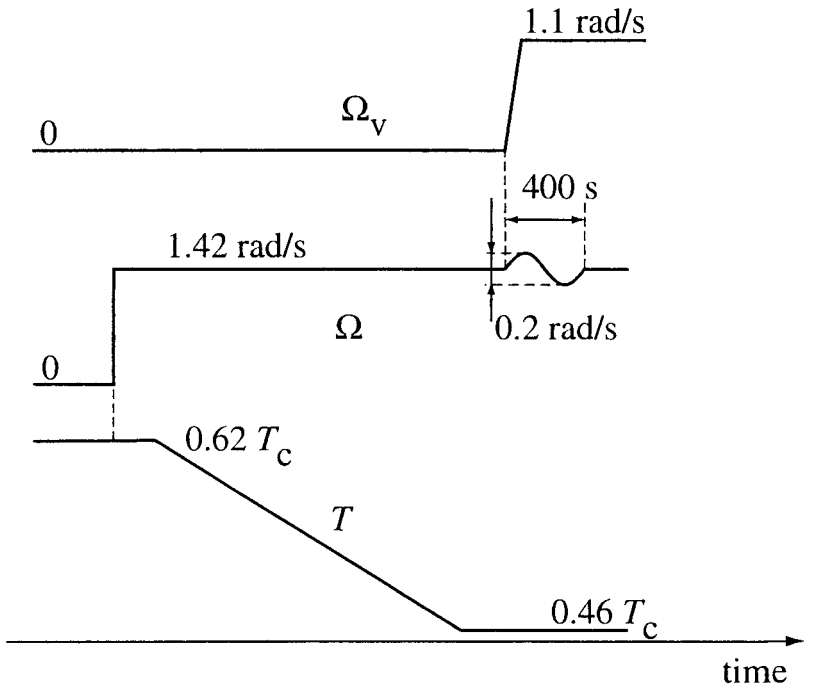

Fig. 20. Demonstration of a sudden burst of vortices leaking through the orifice, triggered by accelerating rotation: (Ω) The rotation drive is kept constant, until one period of sinusoidal modulation is superimposed. (T) The temperature is reduced at constant Ω into the region where vortex leakage should have occured according to Fig. 19. (Ω_r) The number of vortices $\propto \Omega_r$ remains zero, independently of the temperature sweep, until acceleration starts. At this point the container is flooded by vortex lines. Container #1 has been used at a pressure of 21.0 bar.

usual in the superflow through a submicron-size orifice. Their extreme form, a near total collapse of the flow, has been the subject of recent experiments.[60] Such events appear to be more frequent at low temperatures when mutual friction is sufficiently small and dissipative vortex motion is slow. They might be started when two or more vortices are nucleated almost simultaneously, perhaps at competing nucleation sites.

The premature vortex lines in Figs. 14 and 15, which appear before the counterflow velocity has reached its critical value, might also be associated with the orifice of the rotating container. Like the leakage, the presence of the premature steps seems to become more pronounced with increasing orifice size and with increasing pressure.

Vortices generally exist below the orifice at rotation velocities of order 0.1 rad/s, unless the set-up with the two NdFeB magnets is used, as shown

in Fig. 8. In this case the magnetic field of ≈ 0.6 T will keep the ^{3}He liquid between the NdFeB pole pieces in the A phase. All our experiments so far[47] indicate that vortex lines, which would be continuous across an intersecting A-B interface, do not seem to be easily formed. Therefore it is quite likely that in the situation of Fig. 8 vortices do not exist in the tube below the orifice unless they have leaked from the container. The NdFeB magnets were present only in the measurements with the quartz container.

2. *Remanent Vortices*

Trapped vorticity plays an important role in ^{4}He-II, but in ^{3}He-B it is expected to be less decisive, owing to the large radius ($\lesssim 100$ nm) of the singular core and weak pinning. This argument is confirmed by the present measurements: There is no indication of trapping in the smooth-walled containers (#1 and 4), provided that the vorticity has been allowed to decay in stand-still for a few minutes after rotation has been stopped. Primordial trapped vortices, which would have been created during a transition into the superfluid state while the cryostat was not rotating, were not observed in any of the containers. In the case of ^{4}He-II, reports of remanent vorticity are frequent even in the virgin state, obtained by cooling nonrotating liquid through T_λ.[3,13,61] Rapidly quenched transitions into the superfluid state in zero flow conditions have lately been a subject of interest because of their similarity to cosmological phase transitions. They have been found to lead to a dense vortex tangle in ^{4}He.[62]

In the rough-walled containers #2 and 3 remanent vorticity, trapped in surface porosity, is observed after vortex lines have been annihilated. In Fig. 21 four recorder traces are plotted of the Larmor peak height while Ω is increased from zero at constant rate. Container #2 has been used, in which remanent vorticity is most conspicuous. For reference, the lowest trace is the virgin state, as in Figs. 14, 15 and 16. The 3 traces above it represent different cases with remanent vortices. Here the cryostat has previously been rotated with N_a vortex lines. These have then been annihilated during deceleration to $\Omega = 0$, whereby some traps on the cylindrical wall are loaded. The absorption during the subsequent acceleration is plotted as function of Ω.

Two features in Fig. 21 are of interest to us here: 1) At low Ω randomly occuring solitary steps are observed which are produced by remanent vortices, mobilized by the accelerating counterflow. 2) Ultimately at higher Ω periodic vortex generation sets in and a more regular staircase pattern follows. The trace for the virgin state differs from those above it: Here there are 1–3 premature steps and then the periodic process starts. Its onset is reproducible and corresponds to the largest possible value of counterflow at given T and P. We take that in this case no remanent vortices exist in

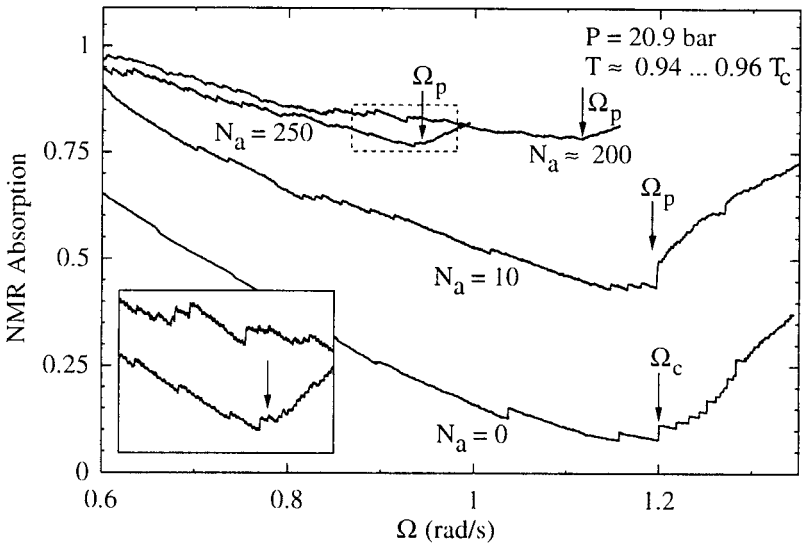

Fig. 21. Vortex lines formed from remanent vorticity as a function of rotation velocity Ω during constant acceleration ($d\Omega/dt = 1 \cdot 10^{-4}$ rad/s^2) at constant T. The remanent vorticity originates from vortex filaments which were trapped on the cylindrical wall when vortices annihilated during earlier deceleration. On the vertical scale is the Larmor peak height, normalized to its value in the nonrotating state. The four traces (*from bottom to top*) correspond to: ($N_a = 0$) Virgin state. ($N_a \neq 0$) After deceleration to zero from an earlier vortex cluster state (with $N_a = 10$, 200, and 250 vortices), rotation is restarted in the same direction. The vertical arrows indicate the onset of periodic vortex generation in accelerating rotation. The *insert* shows a magnified view of the $N_a = 200$ and 250 traces from the region within the box drawn with dashed lines. The randomly occurring steps to the left of the onset in the three upper traces correspond to vortex lines which are formed from trapped remanent filaments. They have to be subtracted to find the proper critical counterflow velocity $v_{cm} = \Omega_{cm} R$ for the onset of the periodic process. Thus the vertical arrows represent the absolute upper limit for Ω_{cm}. In the case of the two top most traces we clearly have $\Omega_{cm} < \Omega_c$ and the periodic process corresponds to vortex mill behavior. Container #2 was used in these measurements.

the container, *i.e.* all traps on the cylindrical wall are empty. In Fig. 21 the onset point of the periodic process is identified with a vertical arrow. In the virgin state the arrow is at $\Omega = \Omega_c(T, P)$, if we neglect the two premature steps.

From Fig. 21 it is seen that the total number of remanent vortex lines N_r, which are formed during the acceleration, depends on the number of vortex lines N_a, which were annihilated during previous deceleration. This dependence is displayed in Fig. 22. The plot has been generated from a sequence of measurements in isothermal conditions where the procedure is the following: First Ω_c of the virgin state is measured at constant acceleration. Only a few vortices are allowed to nucleate and these are counted

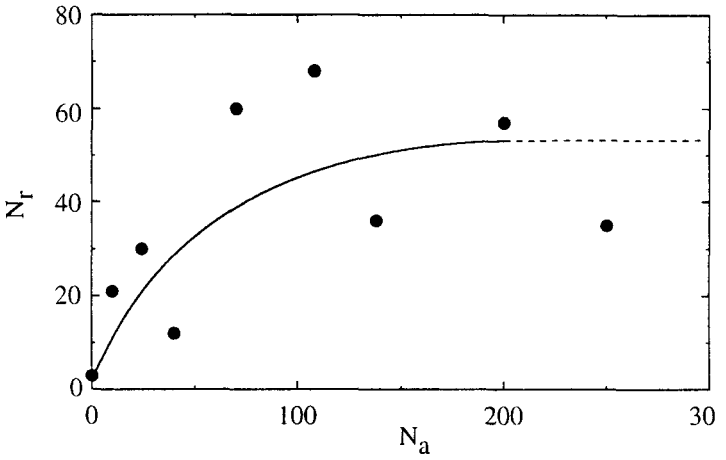

Fig. 22. Total number of remanent vortices N_r, which are randomly mobilized during constant acceleration, before periodic vortex formation sets in. N_r is plotted as a function of N_a, the number of vortices which were annihilated during the last deceleration to zero. The direction of rotation is kept unchanged. N_r first increases and then seems to saturate when all available traps on the cylindrical wall have been loaded with vortex filaments.[63] The results are from measurements similar to those in Fig. 21.

to give N_a for the next round. Then the cryostat is decelerated to zero, rotation is restarted in the same direction, the remanent vortices N_r are counted, the onset of the periodic process is determined, and subsequently rotation is stopped to start the third cycle. In this way we obtain from each cycle the number of remanent vortices N_r, the onset of the periodic process, and from the previous round the corresponding value of N_a. The probability that a trap is loaded with a remanent vortex filament is characterized by the value of N_a. As seen in Fig. 22, initially N_r increases with N_a as expected, when more traps are loaded. At higher values of N_a the dependence seems to saturate, which would be expected if all traps are occupied.[63]

To summarize we note that remanent vortices are released in a stochastic manner with linearly increasing superflow velocity and their number depends on how many vortex lines have been annihilated previously. The traps are supported by surface porosity, consisting of small cavities and asperities (with a size distribution of up to about 0.3 mm in container #2). This is the traditional kind of remanent vorticity, in which one trapped vortex filament will on an average produce one vortex line. If the direction of superflow is reversed, then the probability of the filament becoming mobile decreases and the chances for its total annihilation increase. In increasing superflow, ultimately all traps might be emptied, the

supply of trapped vorticity would be exhausted, and intrinsic nucleation would start at the critical velocity of the virgin state. Instead, as seen in Fig. 21, in container #2 often a periodic process of vortex generation sets in already at a lower counterflow velocity.

3. *Vortex Mill*

In all of the three traces with remanent vortices in Fig. 21, eventually a periodic process starts at some Ω_p. We call the corresponding critical counterflow velocity at the cylindrical wall

$$v_{cm} = \Omega_{cm} R = \Omega_p R - \frac{\kappa N_r}{2\pi R} \tag{37}$$

Beyond the onset Ω_p the counterflow velocity is limited to $\leqslant v_{cm}$ and no more randomly generated remanent vortices are expected to appear. To obtain v_{cm} from Ω_p one has to subtract all the N_r remanent vortex lines. At higher rotation velocities, where the counterflow absorption peak is well developed in the NMR spectrum, the remanent vortex lines can be readily counted from the steps in the absorption record. This gives a minimum estimate of the remanent vortex number, which in turn provides a maximum limit for the counterflow velocity v_{cm} at the onset. This is because at low Ω no steps are yet visible in the spectrum and thus more remanent vortices may have become mobile than one can conclude from the recorded steps. In a situation with trapped vorticity the iterative bracketing method (Sec. III E) for measuring the cluster size may be somewhat unpredictable, since it depends on a sequence of deceleration–acceleration cycles (see example #2 in Fig. 13). The most practical method is to estimate the vortex number from the relative height of the Larmor peak compared to the counterflow peak (cf. Figs. 11 and 12), which also can be used to provide the total number of remanent vortices at Ω_p. We thus get a second estimate of v_{cm}, which is below the strict maximum limit mentioned earlier.

Data for v_{cm} have been collected in Fig. 23 for container #2, along with measurements on $v_c(T, P)$ in the virgin state. The estimate for N_r is here a lower limit which may include an uncertainty of up to 20, because reference line shapes for vortex clusters with a known Ω_c^* were not collected for comparison as a sufficiently fine grid. Nonetheless, many data points for v_{cm}, which are associated with a small value of N_r, agree well with $v_c(T, P)$ measured for the virgin state. This we interpret to mean that once the loaded traps have been emptied, then periodic intrinsic nucleation starts.

The intriguing result, however, is that there are data points for v_{cm} which fall well below $v_c(T, P)$. This conclusion can be asserted with

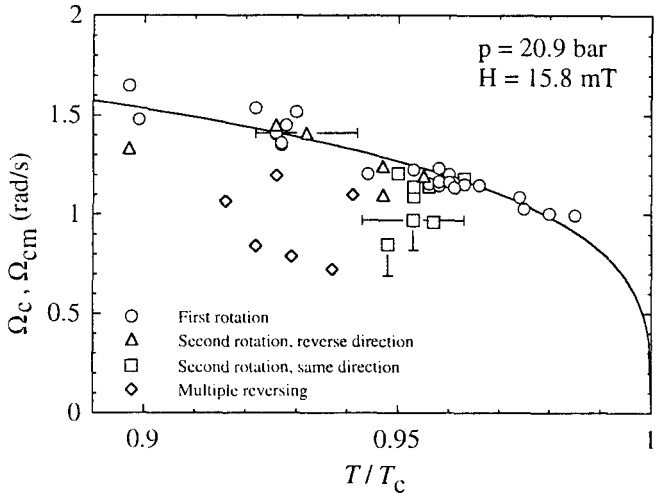

Fig. 23. Critical counterflow velocity (either Ω_c or Ω_{cm}) for the onset of periodic vortex generation in accelerating rotation as a function of temperature: (○) Virgin state with no remanent vortices. Here Ω_c is measured. (*Other symbols*) Onset of periodic process in the presence of remanent vortices. The legend lists the previous history of rotations and subsequent decelerations with an unspecified number of vortices annihilated each time. The horizontal uncertainty bars indicate the typical precision in the temperature measurement. The vertical uncertainty bars are asymmetric around the data point because of the uncertainty in subtracting all randomly mobilized remanent vortices: The plotted value of Ω_{cm} represents an upper limit where the periodic process has clearly set in with a stable limiting counterflow velocity. The solid line denotes the fit to Eq. (38) for Ω_c data with $l = 55\,\mu$m and $\chi = 0.45$. Part of the critical velocity measurements in the presence of remanent vortices display an Ω_{cm} which agrees with Ω_c but others give much lower values and are attributed to vortex mill behavior. The measuring conditions are the same as in Figs. 21 and 22.

confidence since the upper limit of v_{cm} is accurately determined. Such points we attribute to continuous periodic vortex generation from trapped vorticity, known as the *vortex mill*.[64,65] The external features of vortex mill operation, except for the onset value Ω_{cm}, are similar to those of intrinsic nucleation. What we associate with vortex-mill behavior is identified by the following criteria:

(1) The critical velocity v_{cm} of the vortex mill is smaller than v_c and not reproducible from one measuring session to the next, since it is unlikely that exactly the same trapping configuration would be reactivated. Vortices appear as a sequence of single or multiple quantum events such that at $\Omega \geqslant \Omega_p$ the number of vortices generated by the mill is proportional to

$\Omega - \Omega_{cm}$. This means that the active trap is localized to one site on the cylindrical wall. A large critical velocity is associated with the mill, since the data fall in the regime $\frac{1}{2}\Omega_c < \Omega_{cm} \lesssim \Omega_c$.

(2) Like N_r in Fig. 22, the number of randomly mobilized remanent vortex lines during acceleration, also the critical velocity v_{cm} of the vortex mill depends on N_a, the number of vortex lines which were annihilated in the previous measuring session, when the cryostat was decelerated to zero. This is plausible, since more traps suitable for the milling action and among them some with lower critical velocities will have a chance to become loaded, when the number of annihilated vortex lines increases. In Fig. 24 Ω_{cm} is displayed as a function of the previously annihilated vortex lines N_a. The data have been collected while N_r was measured, as described in the context of Fig. 22 in Sec. IVC2. The result is a monotonically decreasing curve as a function of N_a, which extrapolates to $v_c(T, P)$ of the virgin state, when $N_a \to 0$. Evidently the linear dependence should level off with further increase of N_a, but this regime was apparently not reached in the measurement.

The vortex mill can be understood in terms of a trapping geometry which has been proposed by Schwarz.[65] One end of the trapped vortex

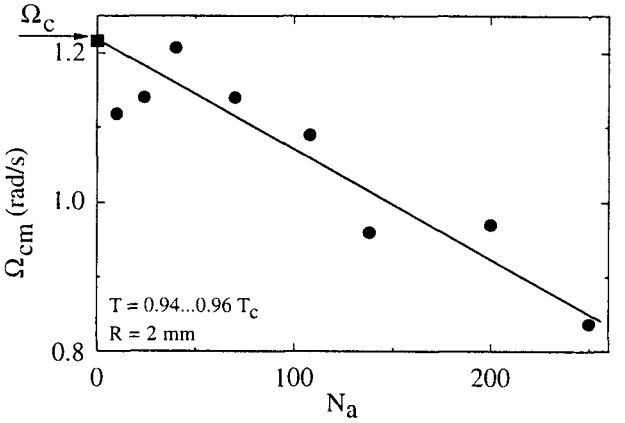

Fig. 24. Critical rotation velocity Ω_{cm} for the onset of periodic vortex formation during constant acceleration at constant T in the presence of trapped vorticity, plotted as a function of N_a, the number of vortices which were annihilated during the previous deceleration. The direction of rotation is kept unchanged. With increasing N_a more traps are loaded and the probability of vortex mill operation at a lower counterflow velocity increases. The monotonically decreasing curve extrapolates to $\Omega_{cm} = \Omega_c$ at $N_a = 0$, *i.e.* to the critical velocity of the virgin state where all traps are empty (Fig. 23). Container #2 has been used and the same measuring conditions apply as in Fig. 22.

filament stays fixed in a region where $v_s \approx 0$. The other end extends into a region with nonzero superflow and starts to expand when the critical velocity v_{cm} is approached. This scenario of a mill is fitting for container #2, where the cylindrical wall is pitted with cavities (Fig. 25). Here a section from a previously annihilated vortex line remains trapped between an asperity on the bottom of a pot-hole and its rim. When the velocity of the counterflow above the cavity increases, the trapped vortex filament expands until it meets the opposite edge of the rim. At that point a vortex loop will be cut off. It expands to a vortex line, and reduces the counterflow velocity. A remnant of the filament is left behind in the pot-hole, which in the reduced counterflow shrinks back to its shortest length and to its original configuration.

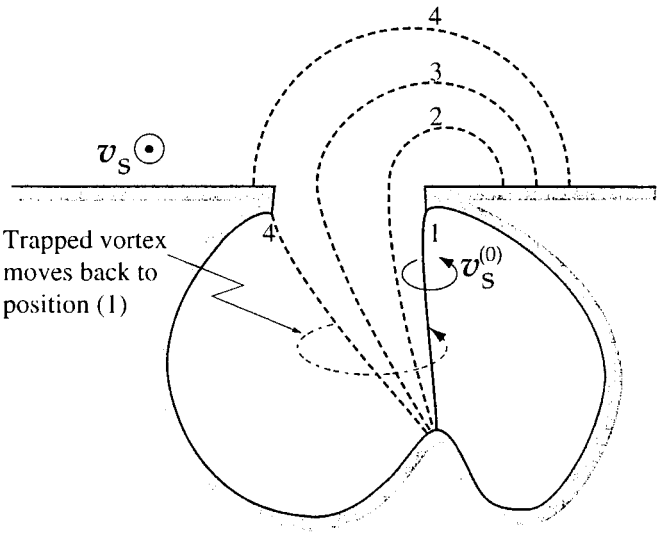

Fig. 25. Illustration of a trap which consists of a cavity on the cylindrical wall of the container, with approximately circular cross section in the plane of the wall. The trap is loaded when a vortex line is annihilated on the wall during decelerating rotation and a section of the line is left behind (*solid line*), stretched between the rim and an asperity on the bottom. In increasing counterflow the filament expands (*dashed lines*) perpendicular to the flow and ultimately intersects with the opposite edge of the rim. At this point a new loop of the size of the cavity is cut off and becomes mobile in the superflow. As a result, the flow velocity in the cavity decreases and the trapped section returns to its original position (*solid line*), where its length is minimized, by sliding around the circular rim of the cavity. In accelerating rotation the process is periodic, as the trapped filament is not able to escape, and thus the trap works as a vortex mill.

Finally we comment on a few more obvious observations. The number of randomly mobilized trapped vortices decreases if the direction of rotation is reversed from what it was before (Fig. 23). In this case a smaller fraction of the trapped vortex filaments are able to expand during rotation in the opposite direction. Presumably these remnants are trapped in a configuration which is roughly transverse to the rotation axis. The pinning force can be estimated from the data in Fig. 20. From other dynamic measurements[45] we can assume that the release of a trapped vortex filament starts at a relatively small change in Ω, since a vortex cluster is set into motion in the rotating state by a step change in Ω which is as small as $\Delta\Omega \approx 0.1$ rad/s, *i.e.* only a small change in Ω is required to start the motion of vortex lines towards a new equilibrium configuration. Thus the critical velocity of a remanent filament is probably determined by when the loop reaches the self-sustained radius $\mathscr{R}_0(v_s)$, which is governed by the local geometry of the trap on the corrugated wall. At lower velocities the filament survives in a trapped metastable state, a local energy minimum stabilized by the line tension.

To summarize, we note that in ^{3}He-B extrinsic mechanisms of vortex formation can be controlled with the design of the experimental setup: With sufficiently smooth walls and a suitable closed geometry, extrinsic effects can be excluded. In containers #1 and 4 no trapped remanent vortices were observed when the cryostat was allowed to stand in rest for several minutes. In container #1 with the largest orifice of 1 mm diameter the chamber was observed to fill in a sudden burst with a large vortex cluster at low temperatures in accelerating rotation. In containers #2 and 3 with rough walls remanent vorticity was prominent, if vortices had previously been annihilated in decelerating rotation.

V. INTRINSIC NUCLEATION MECHANISM

A. Results on Critical Velocity

The measured intrinsic critical counterflow velocity $v_c(T, P) = \Omega_c R$ is shown in Fig. 26. The data are from measurements with container #1, either isothermally at constant slow acceleration ($d\Omega/dt \sim 10^{-3}...10^{-4}$ rad/s^2) or by sweeping temperature at constant Ω. In most cases the critical point was determined from the NMR absorption height, but we have also used the homogenously precessing domain (HPD) mode.[59] In this experiment the signal-to-noise resolution was not sufficient for discerning one single vortex line. Instead the critical velocity was determined from the discontinuity in the slope of the feature which was monitored as a function of the scanned variable (Sec. III E). The good reproducibility of the results, *i.e.* their

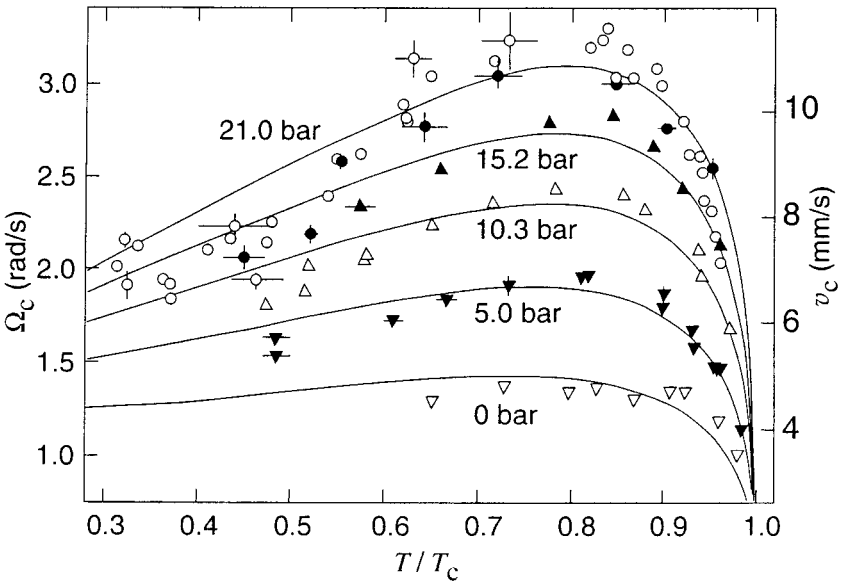

Fig. 26. Critical rotation velocity Ω_c (*left axis*) and flow velocity $v_c = \Omega_c R$ (*right axis*) of intrinsic nucleation in container #1 as a function of temperature T/T_c for pressures $P \leqslant 21$ bar. At 21.0 bar there are two sets of data: (●) ^{3}He with less than 20 ppm of ^{4}He impurity, (○) ^{3}He with ~0.6% ^{4}He. All other data have been measured with the 0.6% mixture. The curves represent Eq. (38) with $\chi = 0.45$ and $l = 3.1\,\mu$m.

independence from the earlier rotation history or the vortex cluster size, provide the justification for associating the data with a well-defined intrinsic critical velocity.

A second example of v_c measurements is shown in Fig. 27, where the quartz container #4 has been used. This experiment concentrates on high temperatures, since only in this region Ω_c is within the reach of the present maximum rotation velocity of 3.5 rad/s for our cryostat. A low NMR field of 11.8 mT is used to provide good frequency resolution close to T_c, where the frequency shifts are small. The measurements have been performed by monitoring the absorption at the counterflow peak while either Ω or T is scanned. In this experiment single-vortex resolution is achieved at vortex-free counterflow velocities of 0.7–2 rad/s, but above 2 rad/s the relative change produced by one vortex line in the counterflow peak height becomes comparable to the noise. The curves in Fig. 27 have been fitted to the data and have approximately $(1 - T/T_c)^{1/4}$ dependence.

On comparing the results from measurements on $\Omega_c(T, P)$ with the different containers, shown in Figs. 23, 26, and 27, two features attract attention: (1) The magnitude of v_c varies by a factor of 4 between Figs. 23

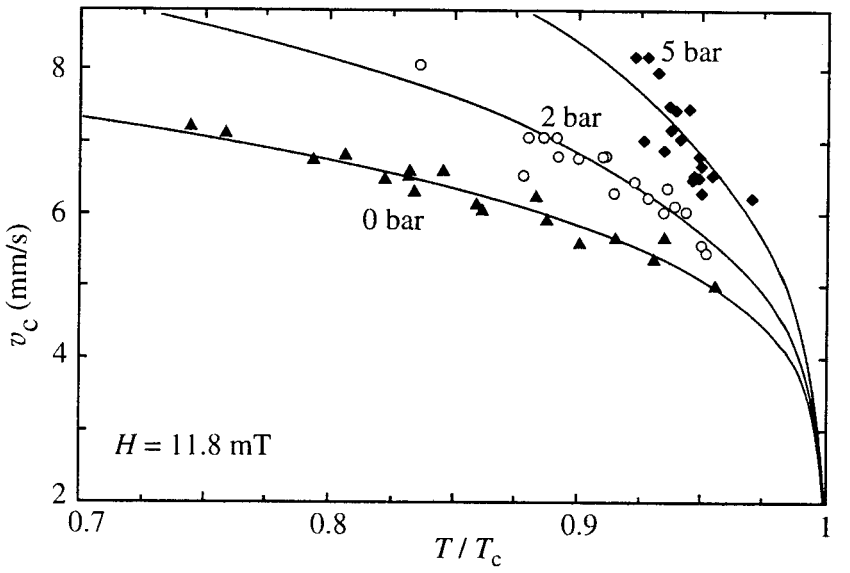

Fig. 27. Critical counterflow velocity v_c of intrinsic nucleation in container #4 as a function of temperature T/T_c for 3 pressures $P \leq 5.0$ bar. The curves represent fits to Eq. (38) with $\chi = 0.45$ and $l = 1.9\ \mu$m, *i.e.* with approximately $v_c \propto (1 - T/T_c)^{0.275}$.

and 27. Thus the measured critical velocity is not a unique quantity, but depends on the sample chamber. This has to reflect the effect of surface roughness, since the containers are otherwise very similar. (2) The dependences of v_c on T and P resemble those of the calculated instability velocity $v_{cb}(T, P)$ of bulk superflow, shown in Fig. 4. The close similarity makes one wonder what is the connection between the two quantities, in spite of the fact that in magnitude v_c and v_{cb} differ by a factor ranging from 3 to 25.

To check for a connection we look for it in the form of a scaling law: the ratio v_c/v_{cb} is equated to some function $f(\xi/l)$ which depends on the temperature and pressure dependent coherence length $\xi(T, P)$ and is parametrized in terms of a length l characterizing surface roughness. In Fig. 28, $\log(v_c/v_{cb})$ has been plotted as a function of $\log \xi(T, P)$ for the different containers. We use the coherence length $\xi(T, P) = \xi_0(P)[\Delta(0)/\Delta(T)]$, with $\xi_0(P) = \sqrt{7\zeta(3)/48\pi^2}\, hv_F/k_B T_c$ and the weak-coupling value for the superfluid energy gap $\Delta(T)$. The data fall on a straight line which is different but approximately parallel for each container and thus we retrieve power law behavior in the simple form

$$v_c = v_{cb}(\xi/l)^{\chi} \tag{38}$$

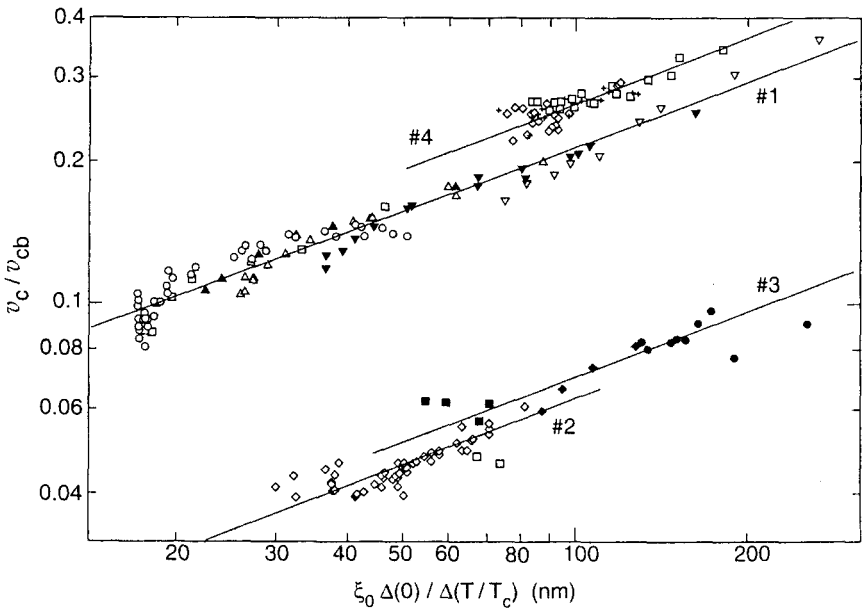

Fig. 28. Equation (38) fitted to $v_c(T, P)$ data measured in the four sample containers (#1–4). Plotting v_c/v_{cb} *vs.* $\xi(T, P)$ (with ξ in nm) on logarithmic axes gives roughly parallel lines for all results. All data from Fig. 26 are included for container #1 and have been denoted with the same symbols. The data for containers #2–4 have been measured with pure ^{3}He at the following pressures: (#2) ◇ 21.0 bar, □ 5.0 bar; (#3) ● 0 bar, ◆ 5.0 bar, ■ 18.0 bar; (#4) □ 0 bar, +2.0 bar, ◇ 5.0 bar. The slopes of the lines determine χ and have been drawn for $\chi = 0.45$. The following values are obtained for the characteristic length l in containers #1–4, respectively: 3.1, 60, 40, and 1.9 μm. The estimates for the large scale limit of surface roughness are correspondingly 2, 300, 30, and $< 1\,\mu$m, as determined visually with a microscope or with a mechanical scanner using a stylus needle.

The result agrees with Eq. (21), if the core radius a is measured in units of ξ. The slope of the lines gives the exponent χ which in the case of container #1 has the value $\chi = 0.45 \pm 0.03$. For other lines the slope is more uncertain and χ might be smaller by a factor of up to 2. In Fig. 28 the lines have been drawn parallel. In this case the intercept of the lines defines the characteristic length l which is different for each container. It proves to be $l = (3.1 \pm 0.3)\,\mu$m for container #1 where the data cover the largest range in temperature and pressure. For the quartz container (#4) with the highest v_c the result is $l = 1.9\,\mu$m, while containers #2 and 3 with low values of v_c yield 60 and 40 μm, respectively. These parameter values have been used to plot the curves in Figs. 23, 26, and 27.

B. Influence of Surface Roughness

One of the very earliest suggestions to explain the small critical velocities measured in ^{4}He-II was to consider the velocity enhancement at sharp surface asperities,[41] as discussed in Sec. IIC2. Since then this explanation has been considered in many reports, in particular by Hess and his coworkers. They have performed a series of measurements on superflow through orifices of mesoscopic size, typically with a diameter of $\sim 10\,\mu$m.[66,67] Convincing evidence for the importance of surface roughness has been hard to demonstrate. In the case of ^{3}He-B the situation is different: From Fig. 28 it is seen that the critical velocity varies from one container to the next. Qualitatively, the sequence of lines in Fig. 28 agrees with what one would expect from the examination of the roughness of the different surfaces (Sec. IIIA), but a quantitative comparison is not straightforward.

In comparing our experimental results to the potential-flow model, as expressed by Eqs. (21) (Sec. IIC2) or (38) (Sec. VA), some comments are in order. The largest reduction factor v_c/v_{c0} is obtained for a sharp "knife-edge" type of defect with $\alpha = 2\pi$, resulting in $\chi = 1/2$. The fitted value, $\chi \approx 0.45$, corresponds to a subtending angle of 32°, which suggests that the experimental situation could be close to an asperity resembling a 2-dimensional wedge.

All measurements in one container can apparently be fitted with one value of l. This property suggests that the flow instability always occurs selectively at the same, most effective nucleation center, which has the sharpest edge combined with the largest l. It is not clear that such behavior can be expected from our containers with random surface structure. More plausible is the alternative that many competing nucleation centers of roughly similar geometry (and roughly equivalent combination of values for χ and l) exist and can be activated at different times, depending on where the instability happens to develop first.

Looking at Figs. 14 and 15 with a clean periodic nucleation behavior, one might guess that once a particular nucleation site has been activated and the flow remains close to the critical threshold, then this site will continue to be reactivated. This is suggested in particular by the recurrent double-quantum nucleation in Fig. 15. Consistent double-quantum events would seem to require a special environment for the nucleation site, a second edge close by, which cuts the expanding vortex loop into two segments. This then would corroborate our guess that the instability keeps developing at the same site if the flow is maintained close to v_c. On the other hand, Figs. 14 and 15 have been measured in the same container #2 and would seem to require different nucleation centers. This, in turn, points to the existence of competing sites.

In experiments on superfluid ^{3}He the boundary properties can be manipulated by adding small amounts of ^{4}He to the ^{3}He sample. Two relevant observations were made in this context. The ^{4}He component phase-separates to a ^{3}He-^{4}He mixture which at low pressures covers all walls as a superfluid film, while the excess collects on the bottom of the ^{3}He volume. The saturation thickness of the film is approximately 30 nm. The film levels out surface roughness on a length scale $\leqslant \xi$ and transforms quasiparticle reflection from diffusive to specular.[68] The results in Figs. 26 and 29 demonstrate that the presence of the ^{4}He component has little influence on the critical velocity v_c. This conclusion is in agreement with theoretical expectation (Sec. IIC1): Small-scale roughness ($l \leqslant \xi$) and diffusive quasiparticle scattering at the wall do not reduce the critical velocity from that in the bulk liquid.

In the second test the ^{3}He rich mixture with roughly 0.6% ^{4}He is rapidly pressurized at $T < 0.3$ K to above 25.0 bar, the solidification pressure of ^{4}He. This means that the superfluid ^{4}He-rich film on the walls of the NMR sample chamber is rapidly brought to a high pressure, while it is simultaneously kept at a low temperature. The idea is to not allow enough time for the film to creep through the orifice, to phase-separate, and to solidify in a few large crystals on the bottom of the ^{3}He volume. Instead one might precipitate the solid phase in micron-size crystallites on the walls

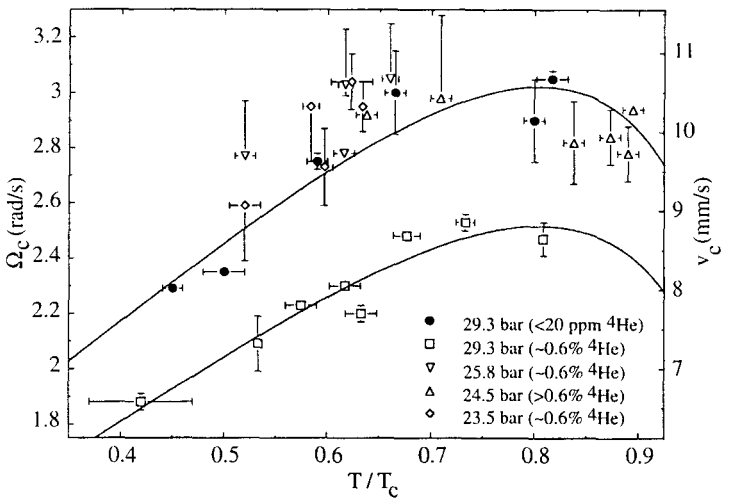

Fig. 29. Ω_c (*left axis*) and v_c (*right axis*) *vs.* T/T_c at higher pressures in container #1. The data (□) for 29.3 bar with 0.6% ^{4}He display a reduced v_c, which suggests that the residue from the solidification of the ^{4}He component on the cylindrical wall increases surface roughness. The two solid curves represent Eq. (38) at 29.3 bar with $\chi = 0.45$ and $l = 3.1\,\mu$m (*top*) or $l = 5.0\,\mu$m (*bottom*).

of the sample container. Such microcrystallites would introduce large scale roughness ($l \gg \xi$) and would provide new nucleation sites during rotation. As seen in Fig. 29, one of the pressurizations to 29.3 bar produced a v_c which is reduced by 20% from that measured for the pure ^{3}He sample (with less than 20 ppm of ^{4}He). In this measurement there were indications that spin-mass vortices[69] were also nucleated, which has not been observed to happen in slow isothermal acceleration otherwise.

Finally, we note that in the present experiments surface roughness is not controlled on the appropriate length scale of $l \sim 1$–$100\,\mu$m. In contrast to ^{4}He-II, in the case of ^{3}He-B it might be possible in principle to perform controlled experiments with quantitative information on the dimensions of the nucleation centers. In practice this is difficult. In all of the containers the edges are rounded and their radius of curvature is much larger than the measured value of l. Thus the corners do not dominate the critical behavior. However, in a rotating container of macroscopic size even a single dust particle or one inadvertent surface defect suffices to determine the critical velocity. A single asperity of a few microns is practically impossible to locate on a surface which is of order 100 mm^2! In the present case the measured characteristic length l correlates qualitatively with the estimated surface roughness of the different containers. On average the quartz container (#4) is much smoother than the best epoxy container (#1), but this difference is not quite apparent in the fitted values of l. Instead the results suggest a defect size which is larger than the nominal roughness of the quartz surface. Here we face the problem with a quantitative comparison with the surface roughness model: Only a positive result, a v_c still closer to $v_{c\hbar}$, would be convincing proof.

To conclude we note that our measurements suggest that surface roughness could be one mechanism responsible for the reduction of the average measured critical velocity v_c from the instability limit $v_{c\hbar}$ of bulk superflow. We cannot exclude the existence of other mechanisms which also might be active in bridging the gap between v_c and $v_{c\hbar}$, although they would have to be of a special kind in the sense that they must obey the scaling law of Eq. (38).

One such additional mechanism was expected to be nucleation induced by background radiation. Close to T_c the critical velocity decreases rapidly with increasing temperature (Fig. 27). Thus by locally heating the superflow the critical threshold can be reduced from that of the surrounding liquid. This can be done with energetic ionizing radiation, such as thermal neutrons or gamma rays. Our measurements show that the absorption of a thermal neutron leads to the nucleation of a vortex ring above some characteristic counterflow velocity $v_{cn}(T, P)$. The ring then expands and forms a vortex line. This process generates single-vortex events at lower

counterflow velocities just above the threshold $v_{cn}(T, P)$ but transforms to double and multiple vortex rings at higher velocities. The maximum available counterflow velocity is limited by the spontaneous critical velocity $v_c(T, P)$.

However, radiation-induced nucleation is not described by Eq. (38). Secondly, long runs of up to 6 h at stable conditions with $v_{cn}(T, P) < v < v_c(T, P)$ were performed to test whether vortex lines were formed in the presence of only the background radiation. Not a single event of that kind was observed. Therefore it does not appear likely that the background radiation is of a suitable kind to reduce the critical counterflow from v_{cb} to v_c within the time it takes to perform a measurement of v_c.

C. Connection with *B* Phase Nucleation

The nucleation of a vortex ring of self-sustainable size at a given superflow velocity is analogous to the problem of nucleating a spherical bubble of ^{3}He-B in ^{3}He-A at a given temperature and magnetic field. The A → B transition is driven by the free energy difference $\Delta F_{AB} = F_A(T, P, H) - F_B(T, P, H)$, which is positive below the thermodynamic transition temperature $T_{AB}(P, H)$. In a homogeneous nucleation process, thermal fluctuations would give rise to a spherical bubble of B phase. The interphasial surface tension $\sigma_{AB}(T, P)$ will cause the bubble to shrink back to zero unless its radius $\mathscr{R}$ exceeds a critical value $\mathscr{R}_c$. The free energy associated with the bubble is

$$F_{nucl} = 4\pi\mathscr{R}^2\sigma_{AB} - \tfrac{4}{3}\pi\mathscr{R}^3\,\Delta F_{AB} \tag{39}$$

Its maximum value

$$F_{\max} = \frac{8\pi}{3}\left(\frac{\sigma_{AB}}{\Delta F_{AB}}\right)^2 \tag{40}$$

represents the nucleation energy barrier with the critical bubble radius

$$\mathscr{R}_c = \frac{2\sigma_{AB}}{\Delta F_{AB}} \tag{41}$$

The numerical values turn out to be large, $F_{\max} \sim 10^6 k_B T_c$ and $\mathscr{R}_c \sim 1\,\mu$m, i.e. of similar magnitude as for a vortex half-ring nucleating in the B phase. As in the case of Eq. (16), with any reasonable attempt frequency ω_0 the probability $\Gamma = \omega_0 \exp(-F_{\max}/k_B T)$ of a thermally activated A → B transition is orders of magnitude below the possible. In effect, the argument here about the impossibility of the A → B transition by any conventional means[70] is similar to that which forbids the nucleation of a vortex

in ^{3}He-B below the bulk superflow instability: In both instances it is basically the very low temperature and the high energy barrier due to the long superfluid coherence length of ^{3}He which make homogeneous nucleation in the bulk liquid unthinkable.

Thus the A phase supercools by large amounts. Nevertheless, it is an experimental fact that eventually one always gets a sudden hypercooled transition into the B phase. There are no heterogeneous or extrinsic nucleation mechanisms of traditional kind which would act in the bulk or at the wall and could initiate the A → B transition. It has been a great puzzle what alternative mechanisms there might exist[70]:

1. Both vortex nucleation and the A → B transition start on the container wall and depend on surface roughness. It has recently been established that in a smooth-walled container the A → B transition is suppressed to unusually low temperatures.[71] In our quartz container (#4), which has the highest critical velocity of our 4 sample chambers, ^{3}He-A supercools in these same measurements well below T_{AB}: at 34.2 bar the transition occurs at $T \approx 0.45T_c$ instead of $T_{AB} = 0.78T_c$ and at 29.3 bar at $0.59T_c$ rather than at $0.85T_c$. One possible explanation[70] is that nucleation starts from the hard core of a point singularity, which is part of a textural defect in the A phase, known as a boojum. It is formed at a sharp surface asperity and might reduce the nucleation barrier of the A → B transition. However, supercooling is independent of the rotational state or the type of vortex structure in ^{3}He-A. Therefore a boojum as the end point of a continuous vortex line does not appear to help in catalyzing the transition.

2. A second common feature of the two nucleation processes is that both can be induced with ionizing radiation. This has been investigated extensively in the case of the A → B transition by Osheroff and his coworkers,[71,72] following the original suggestion of Leggett.[70] Our measurements show that the absorption of a thermal neutron in superfluid ^{3}He-B very effectively nucleates vortex rings at counterflow velocities above some threshold value, which is well below the "spontaneous" v_c of container #4.[73] An absorption event in bulk vortex-free counterflow produces a small volume of heated liquid. When the heated bubble cools back it becomes unstable towards the formation of vortex rings such that, depending on the flow velocity, one or several vortex lines result.

3. History dependence is a third uniting property. In a rough-walled container remanent trapped vorticity gives rise to pronounced

nonreproducibility (Sec. IVC). This is not present in a smooth-walled container. However, the supercooling of the A → B transition is history dependent even in our sample chambers #1 and 4: On cooling from the normal (N) into the A phase, the A → B transition can be supercooled to much lower temperatures than after repeated transitions without visiting the N phase, i.e. an A → B transition, like the last one in the sequence N → A → B → A → B, supercools much less. A remanent textural point defect on the surface might again provide the explanation.

VI. CONCLUSIONS

There are three known stable superfluids: ^{4}He-II, ^{3}He-A, and ^{3}He-B. On general energetic and topological grounds the critical velocity for the nucleation of a segment of a vortex ring is expected to be of order $v_c \sim \kappa/(2\pi a)$ (Eq. (14)), where a is the vortex core radius. In the case of a singular vortex core the length scale of a is the superfluid coherence length ξ. For the continuous vortices in ^{3}He-A it is two or three orders of magnitude larger, i.e. it is either the dipolar healing length ($\sim 10\,\mu$m) or it approaches the intervortex distance (~ 0.2 mm), depending on the value of the magnetic field. On a qualitative level the correlation between the critical velocity and the vortex core radius appears to hold well (Fig. 30), if one compares either the theoretically determined instability limit or the present extrapolated maximum experimental values of the critical velocity for each of the three superfluids.

However, in practice the three superfluids differ greatly with respect to vortex line formation in a rotating container. In ^{4}He-II vortices have a singular core with a diameter of atomic size. Pinning and trapping dominate vortex formation, which takes place at low geometry-dependent critical velocities. Even in the newly formed virgin superfluid, which has been cooled below T_λ in zero superflow conditions, vortices tend to exist as trapped remnants.

The other extreme is ^{3}He-A where the predominant vortex lines have continuous structure and lack a singular core altogether. They are nucleated at very low critical velocities, which are the same for all of our 4 containers, i.e. they are independent of the surface properties.[74]

^{3}He-B is the intermediate case where both extrinsic and intrinsic vortex formation can take place in a rotating container. Depending on the surface structure of the container, one or the other can be arranged to dominate. Measurements with single-vortex resolution allow us to study the reproducibility of the temperature and pressure dependent critical velocity, which then provides the distinction between extrinsic and intrinsic

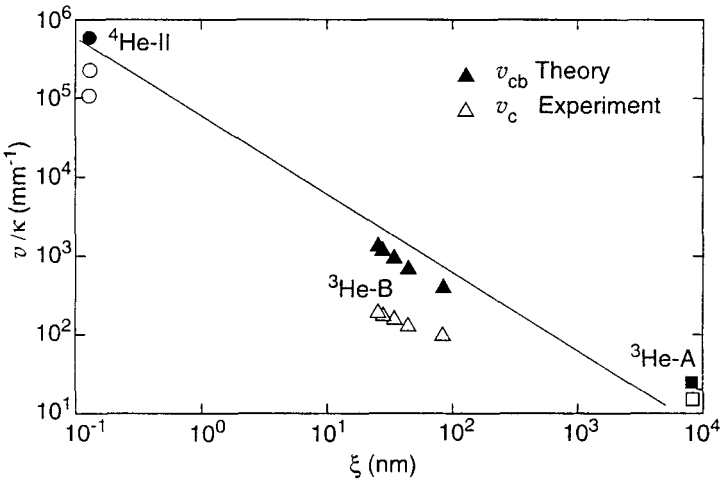

Fig. 30. Theoretically expected velocity of the intrinsic superflow instability v_{cb}/κ (*filled data points*) and maximum measured critical velocity $v_{c,\max}/\kappa$ (*open data points*), plotted for 3 superfluids as a function of the characteristic length scale ξ, applicable to the vortex in each case. The line is a guide for the eye illustrating the order-of-magnitude estimate $v_{cb}/\kappa \propto 1/\xi$.

effects. Extrinsic mechanisms are found to include vortex leakage, proliferation of trapped vorticity, and recurrent vortex-mill operation. In the presence of sufficiently smooth walls intrinsic nucleation proves to be the only available mechanism.

During accelerating rotation, the nucleation of a vortex is observed as a periodic process at a well-defined and reproducible critical counterflow velocity $v_c(T, P)$ at the cylindrical wall. This value is 3 orders of magnitude higher than $\Omega_{c1}R$, at which the first vortex becomes energetically stable in the center of the rotating container. The measured $v_c(T, P)$ is found to be related via a scaling law to the intrinsic instability $v_{cb}(T, P)$ of homogeneous bulk superflow. Surface roughness provides one explanation for the power-law behavior. This interpretation is supported by a simple hydrodynamic model and is augmented by numerical Ginzburg–Landau calculations. Also the surface quality of our four different containers qualitatively agrees in the expected manner with their measured critical velocities.

The scaling law fits both the measurements and the model of velocity enhancement at a surface asperity. This suggests that a nucleation center is singled out on the cylindrical surface, which dominates as the sharpest and tallest protrusion, with a characteristic length $l \gg \xi(T, P)$. Here the counterflow velocity first hits the instability limit $v_{cb}(T, P)$ during the rotational

acceleration. The instability develops to a vortex loop which then expands and finally ends up as a rectilinear vortex line on the periphery of the central vortex cluster.

In ^{3}He-B, three different singular vortex structures have been identified.[31,32] These include the two stable minimum energy structures, a vortex with an axisymmetric core at high temperature and pressure, and a non-axisymmetric double-core vortex at lower temperatures. The present experiments span the range of both of these two vortex structures. Our critical-velocity measurement cannot distinguish between them, since it only determines the onset of the instability, which does not depend on what happens afterwards. The third vortex is a metastable structure, which carries quantized mass and spin supercurrents circulating around the vortex core.[69] This structure requires special conditions for its creation and is generally not formed in the homogeneous counterflow state at low rates of acceleration.

ACKNOWLEDGMENTS

We wish to thank Yu. Bunkov, V. Dmitriev, M. Fogelström, M. Huebner, Y. Kondo, J. Korhonen, and P. Soininen, who have participated in this research extending over many years. We are grateful to O. Lounasmaa, G. Pickett, E. Sonin, E. Thuneberg, and G. Volovik for continued interest and instructive discussions. We would like to express our sincere gratitude to our two anonymous referees who helped to clarify the discussion in this long paper.

This work was supported through the Award for the Advancement of European Science by the Körber Stiftung, by the Academy of Finland, and by the Human Capital and Mobility Programme sponsored by the European Union (under project ULTI–Access to Large Installations No. CHGECT94-0069). NK acknowledges the support from the Russian Foundation for Fundamental Research through the grant No. 96-02-16072; ÜP and VMHR are grateful for scholarships from the Finnish Cultural Foundation and the Wihuri Foundation.

REFERENCES

1. L. Onsager, *Nuovo Cimento Suppl.* **6**, 249 (1949).
2. R. P. Feynman, in *Prog. in Low Temp. Phys.*, Vol. 1, C. J. Gorter (ed.), (North-Holland Publ. Co., Amsterdam (1955), p. 17.
3. R. J. Donnelly, *Quantized Vortices in Helium II*, Cambridge University Press, Cambridge, UK (1991).
4. D. R. Tilley and J. Tilley, *Superfluidity and Superconductivity*, IOP Publishing Ltd, Bristol, UK (1990).
5. W. E. Keller, *Helium-3 and Helium-4*, Plenum Press, New York (1969).

6. Earlier measurements on critical velocities in rotating ^{3}He-B: P. J. Hakonen, *Physica B* **178**, 83 (1992); J. P. Pekola and J. T. Simola, *J. Low Temp. Phys.* **58**, 555 (1985); P. L. Gammel, T.-L. Ho, and J. D. Reppy, *Phys. Rev. Lett.* **55**, 2708 (1985); *ibid.* **52**, 121 (1984); *ibid.* **43**, 1332 (1979).
7. The present work is a continuation of the measurements in Refs. 30, 33, and 23.
8. G. E. Volovik, Modern problems in condensed matter sciences, in *Helium Three*, W. P. Halperin and L. P. Pitaevskii (eds.), Elsevier, Amsterdam (1990), Vol. 26, p. 27.
9. G. W. Rayfield and F. Reif, *Phys. Rev.* **136**, A1194 (1964).
10. D. R. Allen, R. M. Bowley, and P. V. E. McClintock, *Phys. Rev. Lett.* **36**, 1313 (1976); T. Ellis and P. V. E. McClintock, *Phil. Trans. Roy. Soc. A* **315**, 259 (1985).
11. A. I. Ahonen, J. Kokko, O. V. Lounasmaa, M. A. Paalanen, R. C. Richardson, W. Schoepe, and Y. Takano, *Phys. Rev. Lett.* **37**, 511 (1976).
12. C. A. M. Casteljins, K. F. Coates, A. M. Guenault, S. G. Mussett, and G. R. Pickett, *Phys. Rev. Lett.* **56**, 69 (1986).
13. D. D. Awschalom and K. W. Schwarz, *Phys. Rev. Lett.* **52**, 49 (1984).
14. G. A. Williams, *J. Low Temp. Phys.* **89**, 91 (1992), and references therein.
15. E. Varoquaux, G. G. Ihas, O. Avenel, and R. Aarts, *Phys. Rev. Lett.* **70**, 2114 (1993).
16. W. I. Glaberson and R. J. Donnelly, *Phys. Rev.* **141**, 208 (1966).
17. K. W. Schwarz, *Phys. Rev. Lett.* **64**, 1130 (1990).
18. S. V. Iordanski, *Zh. Eksp. Teor. Fiz.* **48**, 708 (1965) [*Sov. Phys. JETP* **21**, 467 (1965)].
19. J. S. Langer and M. E. Fisher, *Phys. Rev. Lett.* **19**, 560 (1967); J. S. Langer and J. D. Reppy, in *Progress in Low Temperature Physics*, C. J. Gorter (ed.), North-Holland, Amsterdam (1970), Vol. 6, p. 1.
20. P. W. Anderson, *Rev. Mod. Phys.* **38**, 298 (1966).
21. G. G. Ihas, O. Avenel, R. Aarts, R. Salmelin, and E. Varoquaux, *Phys. Rev. Lett.* **69**, 327 (1992); S. Burkhart, M. Bernard, O. Avenel, and E. Varoquaux, *Phys. Rev. Lett.* **72**, 380 (1994); O. Avenel, G. G. Ihas, and E. Varoquaux, *J. Low Temp. Phys.* **93**, 1031 (1993); E. Varoquaux and O. Avenel, *Physica B* **197**, 306 1994.
22. A. Amar, Y. Sasaki, R. L. Lozes, J. C. Davis, and R. E. Packard, *Phys. Rev. Lett.* **68**, 2624 (1992); J. C. Davis, J. Steinhauer, K. Schwab, Yu. M. Mukharsky, A. Amar, Y. Sasaki, and R. E. Packard, *Phys. Rev. Lett.* **69**, 323 (1992); R. E. Packard and J. C. Davis, *Physica B* **197**, 315 (1994).
23. Ü. Parts, V. M. H. Ruutu, J. H. Koivuniemi, Yu. M. Bunkov, V. V. Dmitriev, M. Fogelström, M. Huebner, Y. Kondo, N. B. Kopnin, J. S. Korhonen, M. Krusius, O. V. Lounasmaa, P. I. Soininen, and G. E. Volovik, *Europhys. Lett.* **31**, 449 (1995).
24. P. W. Anderson and G. Toulouse, *Phys. Rev. Lett.* **38**, 508 (1977).
25. C. M. Muirhead, W. F. Vinen, and R. J. Donnelly, *Phil. Trans. Roy. Soc.* **A311**, 433 (1984).
26. P. C. Hendry, N. S. Lawson, P. V. E. McClintock, C. D. H. Williams, and R. M. Bowley, *Phys. Rev. Lett.* **60**, 604 (1988), and references therein.
27. R. M. Bowley, *J. Low Temp. Phys.* **87**, 137 (1992).
28. J. Steinhauer, K. Schwab, Yu. Mukharsky, J. C. Davis, and R. E. Packard, *Phys. Rev. Lett.* **74**, 5056 (1995).
29. K. W. Schwarz, *Phys. Rev. Lett.* **59**, 1167 (1987); *ibid.* **69**, 3342 (1992); *J. Low Temp. Phys.* **93**, 1019 (1993); *Physica B* **197**, 324 (1994).
30. Y. Kondo, J. S. Korhonen, Ü. Parts, M. Krusius, O. V. Lounasmaa, and A. D. Gongadze, *Physica B* **178**, 90 (1992).
31. Experimental reviews on rotating ^{3}He superfluids: P. J. Hakonen, O. V. Lounasmaa, and J. T. Simola, *Physica B* **160**, 1 (1989); M. Krusius, *J. Low Temp. Phys.* **91**, 233 (1993).
32. Theoretical reviews on vortex structures in ^{3}He superfluids: M. M. Salomaa and G. E. Volovik, *Rev. Mod. Phys.* **59**, 533 (1987); G. A. Kharadze, Modern problems in condensed matter sciences, in *Helium Three*, W. P. Halperin and L. P. Pitaevskii (eds.), North-Holland, Amsterdam (1990), Vol. 26, p. 167; G. E. Volovik, *Exotic Properties of Superfluid ^{3}He*, World Scientific Publishing Co., Singapore (1992).
33. Ü. Parts, J. H. Koivuniemi, M. Krusius, V. M. H. Ruutu, and S. R. Zakazov, *Physica B* **194–196**, 771 (1994).

34. P. Mathieu, J. C. Marechal, and Y. Simon, *Phys. Rev. B* **22**, 4293 (1980).
35. V. M. Ruutu, J. J. Ruohio, M. Krusius, B. Plaçais, E. B. Sonin, and Wen Xu, Helsinki Univ. of Techn. Rep. TKK-F-A757 (1996), and to be published.
36. D. Vollhardt, K. Maki, and N. Schopohl, *J. Low Temp. Phys.* **39**, 79 (1980); H. Kleinert, *J. Low Temp. Phys.* **39**, 451 (1980).
37. M. Fogelström, unpublished.
38. D. S. Greywall, *Phys. Rev. B* **33**, 7520 (1986).
39. G. E. Volovik, *Pis'ma Zh. Eksp. Teor. Fiz.* **15**, 116 (1972) [*JETP Lett.* **15**, 81 (1972)].
40. P. I. Soininen and N. B. Kopnin, *Phys. Rev. B* **49**, 12087 (1994).
41. W. F. Vinen, in *Progress in Low Temperature Physics*, C. J. Gorter (ed.), North-Holland, Amsterdam (1961), p. 1; and *Liquid Helium*, Proc. Internat. School of Phys. Enrico Fermi, Course 21, Academic Press, New York (1963), p. 336.
42. L. D. Landau and E. M. Lifshitz, *Fluid Mechanics*, 2nd ed. Pergamon Press, Oxford (1987), p. 23.
43. R. E. Packard and T. M. Sanders, Jr., *Phys. Rev. Lett.* **22**, 823 (1969); *Phys. Rev. A* **6**, 799 (1972).
44. H. E. Hall, *Adv. Phys.* **9**, 89 (1960).
45. M. Krusius, J. S. Korhonen, Y. Kondo, and E. B. Sonin, *Phys. Rev. B* **47**, 15 113 (1993-II); *Europhys. Lett.* **22**, 125 (1993).
46. Wen Xu, B. Plaçais, V. M. Ruutu, and M. Krusius, in *Proc. 21 Inter. Conf. Low Temp. Phys.*, S. Danis, V. Gregor, and K. Zaveta (eds.), *Czech. J. Phys.* **46** Suppl., Pt. S1, p. 11 (1996).
47. M. Krusius, E. V. Thuneberg, and U. Parts, *Physica B* **197**, 376 (1994).
48. K. W. Schwarz, *Phys. Rev. Lett.* **47**, 251 (1981).
49. N. B. Kopnin and M. M. Salomaa, *Phys. Rev. B* **44**, 9667 (1991).
50. N. B. Kopnin and A. V. Lopatin, *Phys. Rev. B* **51**, 15291 (1995).
51. T. D. C. Bevan, A. J. Manninen, J. B. Cook, A. J. Armstrong, J. R. Hook, and H. E. Hall, *Phys. Rev. Lett.* **74**, 750 (1995); *Physica B* **210**, 251 (1995).
52. V. M. H. Ruutu, J. H. Koivuniemi, Ü. Parts, A. Hirai, and M. Krusius, *Physica B* **194–196**, 159 (1994).
53. D. Vollhardt and P. Wölfle, *The Superfluid Phases of Helium* 3, Taylor & Francis, London (1990).
54. P. J. Hakonen, M. Krusius, M. M. Salomaa, R. H. Salmelin, J. T. Simola, A. D. Gongadze, G. E. Vachnadze, and G. A. Kharadze, *J. Low Temp. Phys.* **76**, 225 (1989).
55. J. S. Korhonen, Yu. M. Bunkov, V. V. Dmitriev, Y. Kondo, M. Krusius, Yu. M. Mukharskiy, Ü. Parts, and E. V. Thuneberg, *Phys. Rev. B* **46**, 13983 (1992).
56. J. S. Korhonen, A. D. Gongadze, Z. Janu, Y. Kondo, M. Krusius, Yu. M. Mukharsky, and E. V. Thuneberg, *Phys. Rev. Lett.* **65**, 1211 (1990).
57. H. N. Scholz, *Ph.D. Thesis*, Ohio State University, Columbus, Ohio (1981); R. F. Hoyt, H. N. Scholz, and D. O. Edwards, *Physica B* **107**, 287 (1981).
58. A. I. Ahonen, M. Krusius, and M. A. Paalanen, *J. Low Temp. Phys.* **25**, 421 (1976).
59. Yu. M. Bunkov, V. V. Dmitriev, Y. Kondo, J. Korhonen, M. Krusius, Yu. M. Mukharsky, and U. Parts, *Physica B* **194–196**, 761 (1994).
60. O. Avenel, M. Bernard, S. Burkhart, and E. Varoquaux, *Physica B* **210**, 215 (1995).
61. E. J. Yarmchuk and R. E. Packard, *J. Low Temp. Phys.* **46**, 479 (1982).
62. P. C. Hendry, N. S. Lawson, R. A. M. Lee, P. V. E. McClintock, and C. D. H. Williams, *Physica B* **210**, 209 (1995); *Nature* **368**, 315 (1994); *J. Low Temp. Phys.* **93**, 1059 (1993).
63. It is also possible that, instead of saturating, N_r may start to decrease at large N_a. This would be the case if all traps with a low critical velocity are loaded and simultaneously with increasing N_a the onset of the periodic process decreases, as shown in Fig. 24.
64. W. I. Glaberson and R. J. Donnelly, *Phys. Rev.* **141**, 208 (1966).
65. K. W. Schwarz, *Phys. Rev. Lett.* **64**, 1130 (1990); *ibid.* **71**, 259 (1993).
66. Y. J. Brown and G. B. Hess, *J. Low Temp. Phys.* **49**, 267 (1982), and references therein.
67. G. M. Shifflett and G. B. Hess, *J. Low Temp. Phys.* **98**, 591 (1995).
68. S. M. Tholen and J. M. Parpia, *Phys. Rev. Lett.* **68**, 2810 (1992); D. Kim, M. Nakagawa, O. Ishikawa, T. Hata, T. Kodama, and H. Kojima, *Phys. Rev. Lett.* **71**, 1581 (1993).

69. J. S. Korhonen, Y. Kondo, M. Krusius, E. V. Thuneberg, and G. E. Volovik, *Phys. Rev. B* **47**, 8868 (1993-II); *Phys. Rev. Lett.* **68**, 3331 (1992).
70. A. J. Leggett, *J. Low Temp. Phys.* **87**, 571 (1992), and references therein.
71. P. Schiffer, M. T. O'Keefe, M. D. Hildreth, H. Fukuyama, and D. D. Osheroff, *Phys. Rev. Lett.* **69**, 120 (1992).
72. P. Schiffer and D. D. Osheroff, *Rev. Mod. Phys.* **67**, 491 (1995); P. Schiffer, D. D. Osheroff, and A. J. Leggett, in *Progress in Low Temperature Physics*, Vol. 14, W. P. Halperin (ed.), Elsevier Science Publ., Amsterdam (1995), p. 159.
73. V. M. H. Ruutu, V. B. Eltsov, A. J. Gill, T. W. B. Kibble, M. Krusius, Yu. G. Makhlin, B. Plaçais, G. E. Volovik, and Wen Xu, *Nature* **382**, July, 334 (1996).
74. V. M. Ruutu, J. Kopu, M. Krusius, U. Parts, B. Plaçais, E. V. Thuneberg, and Wen Xu, *Helsinki Univ. of Techn. Rep.* TKK-F-A758 (1996), and to be published.